Accepted Manuscript

Flow regimes in a simplified Taylor-Couette-type flow model

D. Lasagna, O. Tutty, S. Chernyshenko

PII: S0997-7546(15)20054-4
DOI: http://dx.doi.org/10.1016/j.euromechflu.2016.01.001
Reference: EJMFLU 2978

To appear in: *European Journal of Mechanics B/Fluids*

Received date: 4 March 2015
Revised date: 24 October 2015
Accepted date: 5 January 2016

Please cite this article as: D. Lasagna, O. Tutty, S. Chernyshenko, Flow regimes in a simplified Taylor-Couette-type flow model, *European Journal of Mechanics B/Fluids* (2016), http://dx.doi.org/10.1016/j.euromechflu.2016.01.001

Flow regimes in a simplified Taylor-Couette-type flow model

D. Lasagna[a], O. Tutty[a,*], S. Chernyshenko[b]

[a] *Engineering and the Environment, University of Southampton, Highfield, Southampton, SO17 1BJ*
[b] *Department of Aeronautics, Imperial College London, Prince Consort Road, London, SW72 AZ*

Abstract

In this paper we introduce a simplified variant of the well-known Taylor-Couette flow. The aim is to develop and investigate a model problem which is as simple as possible while admitting a wide range of behaviour, and which can be used for further study into stability, transition and ultimately control of flow. As opposed to models based on ordinary differential equations, this model is fully specified by a set of partial differential equations that describe the evolution of the three velocity components over two spatial dimensions, in one meridian plane between the two counter-rotating coaxial cylinders. We assume axisymmetric perturbations of the flow in a narrow gap limit of the governing equations and, considering the evolution of the flow in a narrow strip of fluid between the two cylinders, we assume periodic boundary conditions along the radial and axial directions, with special additional symmetry constraints. In the paper, we present linear stability analysis of the first bifurcation, leading to the well known Taylor vortices, and of the secondary bifurcation, which, depending on the type of symmetries imposed on the solution, can lead to wave-like solutions travelling along the axial direction. In addition, we show results of numerical simulations to highlight the wide range of flow structures that emerge, from simple uni-directional flow to chaotic motion, even with the restriction placed on the flow.

Keywords: Taylor-Couette flow, flow regimes, flow stability, bifurcation

*Corresponding author
Email address: o.r.tutty@soton.ac.uk (O. Tutty)

1. Introduction

The flow in the gap between two independently rotating coaxial cylinders, the Taylor-Couette (TC) flow, has been the subject of extensive research work from the early works of Taylor (1923). Because of its simple configuration, it has been a useful ground for comparison between numerical, experimental and theoretical studies, of which a detailed review is beyond the scope of this paper. Because of the large parameter space, defined by the rotation rates of the two cylinders, the ratio of the gap to the span of the cylinder and the ratio of the radii, the TC flow displays a rich phenomenology of flow regimes and bifurcations leading to turbulence, Chossat and Iooss (1985), as exemplified by the experimental work of Andereck et al. (1986) and the early studies of Coles (1965).

When a narrow gap limit of the governing equation is considered, the equations become structurally similar to that of the rotating plane Couette flow, which has also been subject of extensive work, see for example the numerical investigations of Bech and Andersson (1996, 1997) and the more recent study of Tsukahara et al. (2010). The flow is governed by two nondimensional parameters defining the shear rate and the rotation rate, Nagata (1986). For the plane Couette flow with system rotation, the characteristics of the first bifurcation of this system are well known, and the theoretical stability predictions of the linearised equations are in very good agreement with the experimental observation. The laminar Couette flow establishing between the two rigid boundaries shows a first supercritical bifurcation, that results in the formation of azimuthal roll cells. For this case, it is well known, as discussed by Lezius and Johnston (1976), that the conditions for marginal stability for the rotating system have a complete analogy with the buoyancy driven instability in heated fluid layers. For larger values of the governing parameter, the azimuthal toroidal vortices become unstable to a class of non-axisymmetric time-dependent and time-independent disturbances, Nagata (1986), Nagata (1988) and Andereck et al. (1983). Interestingly, some of these three-dimensional nonlinear states survive to the limit of rotation going to zero, i.e. plane Couette flow, Nagata (1990); Faisst and Eckhardt (2000). These tertiary states subsequently undergo a complex sequence of bifurcations, Nagata (1998), leading to a large variety of flow regimes Tsukahara et al. (2010).

The high-Reynolds number turbulent regime as been also extensively studied, for

instance with the purpose of establishing asymptotic scaling laws for the transport of angular momentum Eckhardt et al. (2007); Paoletti and Lathrop (2011); Grossmann and Lohse (2011); Huisman et al. (2012); Busse (2012). At high Reynolds numbers, two- as well three-dimensional large scale organised flow structures still persist, showing hysteretic behaviour, Huisman et al. (2014), and are known to significantly affect the turbulent transport of momentum across the gap, Martínez-Arias et al. (2014); Ostilla-Mónico et al. (2014); Salewski and Eckhardt (2015); Ostilla-Mónico et al. (2015); Brauckmann et al. (2015).

The main contribution of this paper is the discussion of a particular reduced variant of the Taylor-Couette flow. The model that we describe is derived from the original three-dimensional problem by introducing a number of simplifying assumptions, with the objective of making its mathematical analysis as simple as possible. In fact, it should be regarded mainly as a test bed for developing novel analysis methods for studies on stability, transition, turbulence and chaos rather than as a realistic model of the bifurcations and flow regimes of the full three-dimensional problem. As opposed to other TC models based on a system of ordinary differential equations, e.g. Kuhlmann (1985), the model we introduce here is given by a set of partial differential equations that describe the evolution of purely axisymmetric perturbations of the laminar flow, in a narrow gap limit of the governing equations. The main difference with earlier works, e.g. Barenghi and Jones (1989), is the adoption, for the unique sake of further simplification, of periodic boundary conditions along both the radial and axial directions, and the addition of special symmetries to constrain the solution of the problem. For instance, adoption of these peculiar boundary conditions allows an analytical solution of the linear and energy stability problems, whereas these require a numerical solution in the more common case of no-slip boundary conditions. The proposed TC-type flow variant adds to the class of simple flows rich in features and flow regimes, which play a special role in fluid dynamics, as for instance, the Kolmogorov flow, or the ABC flow.

Our motivation for developing and analysing this bare bone version of the TC problem lies in our interest in developing novel methods for stability and control of fluid flows, exploiting the so-called sum-of-squares-of-polynomials optimisation and semi-definite programming techniques, (see Chernyshenko et al. (2014) and reference therein for an intro-

duction to the topic). In particular, a novel approach to nonlinear stability, i.e. stability to arbitrary finite amplitude perturbations, extending the methodology recently proposed in Goulart and Chernyshenko (2012), has been applied on this system, Huang et al. (2015). The objective of this paper is to discuss important characteristics of this system, and in particular to present and discuss the unique flow regimes that emerge in numerical simulations of the problem. Where possible, connection between the presently-observed states and the original three-dimensional flow will be made.

In section 2 the model flow is derived and the numerical approach developed to solve it is discussed. Section 3 contains analytical results of the linear stability analysis of first bifurcation that the flow model exhibits. In section 4 we present numerical results of nonlinear simulations of the flow with two different sets of symmetry constraints that can be imposed on the solution, discussed in section 2. The objective of this section is to show the characteristic flow features that the proposed flow model exhibits and to discuss the differences with respect to the full Taylor-Couette flow. In addition, the stability of the secondary flow is also analysed.

2. Problem definition and numerical methods

A sketch of the flow geometry is given in figure 1, where the flow between two cylinders of radii R_1 and R_2 is considered. We adopt a thin gap approximation of the problem, such that the gap ΔR is small compared to the cylinders radii. The two cylinders rotate with angular speeds ω_1 and ω_2. The frame of reference, fixed in space, is (ξ, r, θ), which are the axial, the radial and the azimuthal coordinates, respectively.

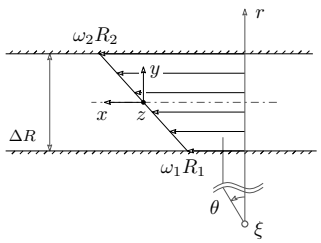

Figure 1: Schematic representation of the physical problem, with the coordinate system adopted.

In an effort to maximally simplify the resulting model of partial differential equations, we do not consider the flow across the full width of the gap, but we study the evolution

of the flow only in a layer of small thickness $\delta \ll \Delta R$ lying in the middle of the gap, at $r = R_1 + \Delta R/2$. We then introduce a rotating frame of reference $\mathbf{x} = (x, y, z)$ centred in the mid-plane between the cylinders, as illustrated in figure 1, which rotates around ξ with angular speed $\omega_R = (\omega_1 + \omega_2)/2$, the angular speed of the layer of fluid in the mid plane. In this frame of reference, x is the streamwise direction, y is the radial direction, while z is the axial direction, with opposite direction to ξ. As a result, a Coriolis force term appears in the equations of motion together with a constant, centrifugal, radial pressure gradient, which can be safely incorporated into the pressure variable.

Under this frame of reference, the problem has a steady laminar solution described by a linear profile, $\mathbf{U} = (by, 0, 0)$, where the slope b is $(\omega_2 R_2 - \omega_1 R_1)/\Delta R$. The linear profile will be referred to as the Couette flow. We consider the evolution of the velocity perturbations $\mathbf{u} = (u, v, w)$ over this basic state.

Along the axial direction z we assume periodic boundary conditions. Although extensive research has established that the domain size might profoundly affect the behaviour of the solution, the preferred wavelength of the roll-cell structures, and the averaged fluxes of momentum/heat, we fix in this paper the z-period to be equal to be thickness δ for the sake of simplicity. On the inner and outer boundaries of the layer of thickness δ we assume periodic boundary conditions for the velocity perturbation vector $\mathbf{u}$. This choice is motivated mainly by the technical reason of constructing a model problem that is more amenable to mathematical analysis, so that the resulting partial differential equations can be used as a more flexible test bed for developing new analysis methods, although the connection with the flow physics of the three-dimensional problem is partially lost. For instance, the linear and energy stability problems can be solved analytically, whereas a numerical solution is required for the more common case of no-slip conditions. This property was indeed exploited in Chernyshenko et al. (2014) and Huang et al. (2015), where a novel method for nonlinear stability analysis was developed and tested on the present flow model.

A further simplifying assumption is that we consider axisymmetric perturbations, for which $\partial/\partial x = 0$. As a result, because the perturbation is independent from x, the evolution of the three-dimensional velocity vector $\mathbf{u}$ in a single two-dimensional axial-radial plane $(z - y)$ is studied. It is important to point out that this assumption has

a profound impact on the flow patters and nonlinear states that are observed in the present flow model, some of which are significantly different from those observed in three dimensional geometries. For example, some of the presently-observed flow regimes are a unique feature of the model and might be overwhelmed by other three dimensional states in a complete configuration. In fact, bifurcations leading to tertiary three-dimensional states, such as wavy vortex cells, Tsukahara et al. (2010), cannot arise in the present model.

Among the different possibilities of normalising the problem, we make velocities non-dimensional as $\mathbf{u}' = \mathbf{u}/\mathrm{d}U = \mathbf{u}/b\delta$, where $\mathrm{d}U = b\delta$ is the mean velocity difference between the inner and outer boundaries of the layer of fluid considered. Lengths are made non-dimensional using $\delta/2\pi$, such that $\mathbf{x}' = 2\pi\mathbf{x}/\delta$, and the domain $\mathscr{V}$ extends in both z and y from zero to 2π. Time is made non-dimensional using a shear based scaling as $t' = t\mathrm{d}U/\delta = tb$.

A natural definition of the Reynolds number, which follows the adopted normalisation, uses the velocity difference $\mathrm{d}U$ and the layer thickness δ, resulting in

$$Re = \frac{\mathrm{d}U\delta}{\nu} = \frac{b\delta^2}{\nu}. \tag{1}$$

Due to the introduction of the rotating frame of reference, a nondimensional parameter expressing the rotation is introduced. The nondimensional number Ω is defined as:

$$\Omega = \frac{\omega_R}{\omega_1} = \frac{1}{2}\frac{\omega_1 + \omega_2}{\omega_1} \tag{2}$$

and it is half the ratio between the angular speed of the mid-plane layer of fluid, to which the coordinates system $\mathbf{x}$ is fixed, and the angular speed of the inner cylinder. This parameter is commonly referred to as the rotation number, as in Lezius and Johnston (1976), Tsukahara et al. (2010).

As mentioned above, the model discussed in this paper is, except for the specific boundary conditions adopted, similar to the well known rotating plane Couette flow (RPC), i.e. the flow between two parallel plates separated by a distance $2h$, moving in opposite direction with relative speed $2U$ and subject to a global angular velocity Ω_z, oriented in the spanwise direction. This configuration is fully characterised by two non-dimensional parameters, (see Tsukahara et al. (2010)), namely the Reynolds number

$Re = Uh/\nu$ and a rotation number $\Omega' = 2\Omega_z h^2/\nu$, based on the viscous time scale h^2/ν. The definition of the Reynolds number in the cited work is equivalent to the one we use in this paper, as given by equation (1), up to a factor of four. On the other hand the scaling of the system rotation in Tsukahara et al. (2010) is slightly different to the one given by equation (2). In particular, the latter is a shear rate based definition, while the former separates better the wall-velocity from the system rotation speed. Nevertheless, the two definition are related by $\Omega = \Omega'/Re$.

A few special cases for Ω can be considered and are here discussed since they are relevant in the rest of the paper. If $\Omega < 0$, the two cylinders rotate with opposite directions, but the outer cylinder rotates faster, and the flow in the middle of the gap is stable to axisymmetric perturbations according to Rayleigh criterion, which is a sufficient condition for stability to axisymmetric perturbation, such as those considered in this problem. This region of the parameter space corresponds to the region of cyclonic rotation in RPC flow, where the rotation of the system has the same sign of the vorticity in the shear layer, and it it stabilising. The transition at high Reynolds number in this region does not result in the growth of two dimensional roll cells but is inherently three-dimensional and shows the appearance of localised steady turbulence spots, as discussed in Tsukahara et al. (2010).

For $\Omega = 0$ the two cylinders rotate in opposite directions with equal angular speed. Thus, the mid plane layer of fluid is at rest and it is not subject to centrifugal forces. This condition is equivalent to that of the plane Couette flow, for which the Reynolds number at which turbulent motion can be sustained lies between 320 and 360, Tillmark and Alfredsson (1992). Crucially, transition in plane Couette flow is driven by a three dimensional instability. In the present case, it can be proved that, in this condition, for no rotation the system is globally stable at all Reynolds numbers, i.e. stable to finite amplitude perturbations. The simple proof is presented in section 3, after the results of linear stability analysis.

If $\Omega \geq 1$, both cylinders rotate in the same direction and the outer cylinder rotates faster, (they rotate at the same speed if $\Omega = 1$). This is a globally stable condition at all Reynolds numbers due to Rayleigh criterion $\partial(r^2u^2)/\partial r > 0$ being satisfied, where r is a radial coordinate and u is the azimuthal component. Therefore, the region of instability

is $\Omega \in (0, 1)$, which we will deal with in the rest of the paper.

Following the assumptions introduced above, the equations governing the dynamics of the perturbation velocity vector $\mathbf{u} = (u, v, w)$ over the Couette flow are

$$\frac{\partial u}{\partial t} + v\frac{\partial u}{\partial y} + w\frac{\partial u}{\partial z} + v = \Omega v + \frac{1}{Re}\nabla^2 u, \tag{3}$$

$$\frac{\partial v}{\partial t} + v\frac{\partial v}{\partial y} + w\frac{\partial v}{\partial z} = -\Omega u - \frac{\partial p}{\partial y} + \frac{1}{Re}\nabla^2 v, \tag{4}$$

$$\frac{\partial w}{\partial t} + v\frac{\partial w}{\partial y} + w\frac{\partial w}{\partial z} = -\frac{\partial p}{\partial z} + \frac{1}{Re}\nabla^2 w, \tag{5}$$

for the azimuthal, radial and axial directions, respectively. The term $+v$ in the first equation is the only contribution from the base flow remaining after the decomposition of the velocity in base flow plus perturbation. In these equations, the Laplacian is defined as

$$\nabla^2 = \frac{\partial^2}{\partial y^2} + \frac{\partial^2}{\partial z^2}.$$

Furthermore, the velocity perturbations are subject to the solenoidal condition $\partial v/\partial y + \partial w/\partial z = 0$.

A convenient reformulation of the problem can be obtained by using the azimuthal component of the vorticity vector, $\omega = \partial w/\partial y - \partial v/\partial z$. In addition, the streamfunction on the axial-radial (z, y) plane, defined by

$$v = \frac{\partial \psi}{\partial z}, \qquad w = -\frac{\partial \psi}{\partial y},$$

can be introduced and it is related to the azimuthal vorticity by the Poisson equation $\nabla^2\psi = -\omega$. The evolution equations for the azimuthal velocity and azimuthal vorticity are

$$\frac{\partial u}{\partial t} + \frac{\partial \psi}{\partial z}\frac{\partial u}{\partial y} - \frac{\partial \psi}{\partial y}\frac{\partial u}{\partial z} = \frac{\partial \psi}{\partial z}(\Omega - 1) + \frac{1}{Re}\nabla^2 u, \tag{6}$$

$$\frac{\partial \omega}{\partial t} + \frac{\partial \psi}{\partial z}\frac{\partial \omega}{\partial y} - \frac{\partial \psi}{\partial y}\frac{\partial \omega}{\partial z} = \frac{\partial u}{\partial z}\Omega + \frac{1}{Re}\nabla^2 \omega. \tag{7}$$

This formulation will be used throughout in this paper.

The flow model presented in this paper is similar to that used by Speziale and Wilson (1989), except for the adoption of periodic boundary condition. As it will be discussed

in section 3, for these boundary conditions the linearised version of (6, 7) produces normal modes that can grow unbounded in nonlinear simulations above a certain critical Reynolds number. To suppress these modes, and to construct systems that have different properties, we define and apply symmetry constraints on the solution of the governing equations. We consider two different sets of constraints. In the first set, symmetries are applied along the radial direction only and, in particular, the azimuthal component u is assumed odd along y. As a result, the equations of motion imply that the radial component v, as well as the streamfunction, are also odd along y, while for continuity w is even on y. This corresponds to:

$$u(-y,z) = -u(y,z) \quad \text{and} \quad \psi(-y,z) = -\psi(y,z). \tag{8}$$

One of the side effects of enforcing this symmetry constraints is that only the flow in one half of the domain, for example in the lower half $\tilde{\mathscr{V}} = [0,2\pi]\times[0,\pi]$, ($0 \le z \le 2\pi,\ 0 \le y \le \pi$), needs to be considered. The flow evolution in the other half can be obtained simply as the mirror image. In addition, enforcing u and v to be odd along y can be seen as equivalent to enforcing no-slip boundary conditions on these two components on $y = 0, \pi$, which we will refer to as the lower and upper boundaries, while the constraint $\psi(-y,z) = -\psi(y,z)$ implies a free-slip condition $\partial w/\partial y = 0$ for the axial component.

For the second set of constraints, additional symmetries along the axial direction z complement the constraints along y. In particular, we impose that u/ψ is even/odd along z such that

$$u(y,-z) = u(y,z) \quad \text{and} \quad \psi(y,-z) = -\psi(y,z). \tag{9}$$

The condition on the streamfunction implies that v/w is even/odd along z. As discussed above, because of the additional symmetries, we will consider the flow only in one fourth of the domain, i.e. in the domain $\mathscr{V}^* = [0,\pi]\times[0,\pi]$.

The system with constraints on both directions will be referred to as the fully constrained system, whereas the system with constraints along y only will be referred to as the partially constrained system. The objective of the present paper, is present some of the different states and bifurcations that these two related systems exhibit, trying where possible to make connections between the presently-observed regimes and those pertaining to the full three dimensional problem.

Numerical methods. Due to the assumption that the flow is independent of x, the problem needs to be spatially discretized along y and z only. More importantly, the adoption of periodic boundary condition along both these two directions, allows the introduction of a double Fourier series expansion. The flow variables are thus represented by the Fourier series expansion

$$(u, \omega)(\mathbf{x}, t) = \sum_{\mathbf{k}} (u_{\mathbf{k}}(t), \omega_{\mathbf{k}}(t)) \exp(i\mathbf{k} \cdot \mathbf{x}) \tag{10}$$

where $u_{\mathbf{k}}$ and $\omega_{\mathbf{k}}$ are the Fourier coefficients vectors for the modes corresponding to the discrete wave vector $\mathbf{k} = (j, k)$, $\mathbf{x} = (y, z)$ is the radial-axial coordinate vector and $i := \sqrt{-1}$ is the imaginary unit. The streamfunction ψ is readily obtained within this formulation by algebraic solution of the Poisson equation. Galerkin projection of (10) onto the governing equations, (6 and 7), results in the system of ordinary differential equations for the Fourier coefficients, which is integrated in time by a standard operator splitting technique. The viscous term is treated implicitly using a Crank-Nicholson method, while the non-linear term, the rotation and mean flow terms are all treated explicitly using a second order Adams-Bashfort method. The non-linear term is solved pseudo-spectrally, and the "2/3 truncation" rule, see Canuto et al. (2007), has been implemented to de-alias the calculations. However, in preliminary resolution and validation tests, we generally observed that de-aliasing did not play a significant role and had a negligible effect in well resolved simulations. All the results discussed in the following have been carefully checked to be grid independent, which was proven by running simulations of the system at several different resolutions, Boyd (2001).

It has to be pointed out that the structure of the Navier-Stokes equations guarantees the conservation of symmetries for initial conditions that satisfy the symmetry constraints. However, in numerical calculations with rounding errors and especially when instabilities of the symmetry-preserving solution exist, as it happens to be in the present case, it is necessary to enforce numerically the constraints. In our numerical code, symmetries are applied in physical space at each time integration step by replacing the values of the flow variables at the grid points with appropriate values, such that the flow preserves the desired symmetries, as specified by equations (8) and (9).

3. Linear stability analysis of the first bifurcation

In this section we provide analytic results of linear stability analysis of the velocity perturbations over the Couette flow, i.e. we determine the stability boundary of the first bifurcation. No symmetry constraints are assumed at this stage. Substituting the orthogonal Fourier system

$$(u,\psi)(\mathbf{x},t)=\sum_{\mathbf{k}}(u_{\mathbf{k}},\psi_{\mathbf{k}})(t)\exp(i\mathbf{k}\cdot\mathbf{x}), \tag{11}$$

with $x=(y,z)$ into (6) and (7) with $\omega=-\nabla^2\psi$, results in a set of coupled ordinary differential equations for the coefficients of each Fourier mode $\mathbf{k}=(j,k)$, which, in matrix notation, reads as

$$\frac{\mathrm{d}}{\mathrm{d}t}\begin{bmatrix}u_{\mathbf{k}}\\ \psi_{\mathbf{k}}\end{bmatrix}=\begin{bmatrix}-\|\mathbf{k}\|^2/Re & ik(\Omega-1)\\ ik\Omega/\|\mathbf{k}\|^2 & -\|\mathbf{k}\|^2/Re\end{bmatrix}\begin{bmatrix}u_{\mathbf{k}}\\ \psi_{\mathbf{k}}\end{bmatrix}+\begin{bmatrix}N_{u_{\mathbf{k}}}\\ N_{\psi_{\mathbf{k}}}\end{bmatrix}, \tag{12}$$

where $\|\mathbf{k}\|=\sqrt{j^2+k^2}$ is the magnitude of the discrete wave vector, and where $N_{u_{\mathbf{k}}}$ and $N_{\psi_{\mathbf{k}}}$ represent the energy conserving nonlinear terms, containing convolution sums of the Fourier coefficients.

The linear operator resulting from the truncation of the Fourier spatial discretization of equation (12), and by dropping the nonlinear term, is a block diagonal matrix, where each block is a 2×2 matrix governing the linear evolution of the coefficients of the Fourier mode $\mathbf{k}=(j,k)$. Since the linear operator is block diagonal, there is no linear interaction among Fourier modes, and their evolution is coupled only through the energy-preserving nonlinear term, via triadic interactions.

The eigenvalue analysis of this system is straightforward, since the operator is block diagonal, and can be performed analytically. Each block has two eigenvalues given by:

$$\lambda^{\mathbf{k}}_{1,2}=-\frac{\|\mathbf{k}\|^2}{Re}\pm\frac{k}{\|\mathbf{k}\|}\sqrt{(1-\Omega)\Omega}. \tag{13}$$

One of the two eigenvalues is always negative whereas the other crosses the imaginary axis at the critical Reynolds number

$$Re_L=\frac{\|\mathbf{k}\|^3}{k\sqrt{(1-\Omega)\Omega}}, \tag{14}$$

The associated pair of eigenvectors, which determines the relative amplitude of the coefficients $u_{\mathbf{k}}$ and $\psi_{\mathbf{k}}$, reads as:

$$e^{\mathbf{k}}_{1,2} = \Big(\pm \|\mathbf{k}\| \frac{\sqrt{1-\Omega}}{\Omega}, 1 \Big). \tag{15}$$

Fourier modes for $k = 0$, which corresponds to purely azimuthal-axial motions, i.e. with $v = 0$, are always strictly stable since the off diagonal terms of the system equation (12), which couple the azimuthal velocity and the streamfunction components for each Fourier mode, become identically zero, leaving a negative definite linear operator for those modes.

The first eigenmodes to become unstable as the Reynolds number is increased are those for $k = \pm 1$, $j = 0$, whose eigenvalues cross the imaginary axis for

$$Re = 1/\sqrt{(1-\Omega)\Omega}. \tag{16}$$

The neutral stability boundary for these eigenmodes has a minimum for $\Omega = 0.5$, at $Re_L = 2$, which is the most unstable condition. On the other hand the neutral stability boundary goes to infinity for both $\Omega = 0$ and $\Omega = 1$ and, therefore, the flow is linearly stable at all Reynolds numbers for these two values. However, the growth of the eigenfunctions with $j = 0$ is prevented by the symmetries constraints of equations (8) along the radial direction y. In fact, the Fourier transform of the flow variables posses a similar set of symmetries, which read as

$$u_{-j,k} = -u_{j,k} \quad \text{and} \quad \psi_{-j,k} = -\psi_{j,k}, \tag{17}$$

implying that $u_{0,k} = \psi_{0,k} = 0$, for each k.

The eigenfunctions having $j = 0$ possess a peculiar nature. In physical space they can be represented by the functions

$$(\tilde{u}, \tilde{v}, \tilde{w})^k_{1,2} = (\pm \frac{\sqrt{1-\Omega}}{\Omega} \sin(kz), \sin(kz), 0),$$

where k denotes the flow corresponding to the wave vector $(0, k)$. A special feature of these normal modes is that, since they do not depend on y, because $j = 0$, the nonlinear term of equations (7) and (6) vanishes identically. As a consequence, the evolution of these modes is governed by a set of linear equations and their amplitude grows unbounded

if the critical Reynolds number is exceeded, because the nonlinear transfer of the energy extracted from the mean flow to dissipative, stable modes is prevented. In fully nonlinear numerical simulations of the flow, these modes are observed to grow exponentially and eventually produce a numerical instability due to violation of the CFL conditions, because the perturbation velocities become very large. This feature reflects the definition of the problem and the assumption of periodic boundary conditions along the radial direction. From a physical point of view, the spatial structure of these degenerate modes may be seen as representing the growth of two adjacent Taylor vortices very elongated along the radial direction, which grow unbounded since the evolution of the flow within an infinitesimal strip of fluid of thickness δ in the middle of the gap is considered.

Because the growth of Fourier modes with $j = 0$ is avoided by enforcing constraints along y, the next eigenfunctions becoming unstable are those corresponding to $j = k = \pm 1$, and, therefore, the fully constrained system and the partially constrained system share the same type of instability for what concerns the first bifurcation. As anticipated, we observe that because symmetry constraints in physical space are reflected in analogous symmetry properties for the Fourier coefficients, we consider in the following only modes for $j \geq 1$ and $k \geq 0$. In physical space, the eigenfunctions of the linear stability problem for the constrained systems have the form

$$(\tilde{u}, \tilde{\psi})^{j,k}_{1,2} = \Big(\pm \frac{\sqrt{1-\Omega}\sqrt{j^2+k^2}}{\sqrt{\Omega}} \sin(jy)\cos(kz), \sin(jy)\sin(kz) \Big), \quad j \geq 1, \quad k \geq 0. \tag{18}$$

In figure 2-(a) we show streamlines in the radial-axial plane of the most unstable eigenfunction $(\tilde{u}, \tilde{\psi})^{(1,1)}_1$. Interestingly, the streamlines describe a pattern of four counter-rotating vortices, one per quadrant, with two vortex cells along the radial direction. Other eigenfunctions, for larger j and k define similar vortical patterns, but with a corresponding larger number of vortices. For example, for $j = 2$, a total of four vortex cells are stacked one on top of each other along the radial direction. This result, in stark contrast with the usual way Taylor cells cover the gap, i.e. only one cell forms in the radial direction, is entirely due to the adoption of periodic boundary conditions. In fact, the flow pattern corresponding to one cell across the gap, say with a non-integer radial wave number $j = 1/2$, would not satisfy the periodicity conditions.

In figure 2-(b), the behaviour of the largest eigenvalue corresponding to the eigenfunction shown in figure 2-(a) is reported for $\Omega = 0.5$, which is the most unstable condition.

In fact, the neutral stability boundary for $j = 1, k = \pm 1$, is given by

$$Re_L = \frac{2\sqrt{2}}{\sqrt{\Omega(1-\Omega)}}, \tag{19}$$

and it is shown in panel (c) of figure 2, together with the neutral stability boundary for the unconstrained system of equation (16).

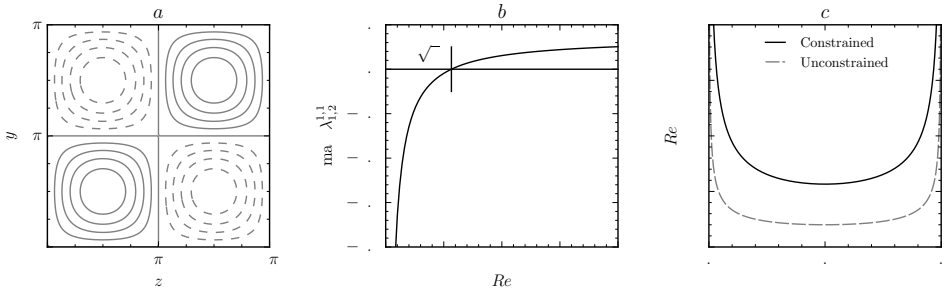

Figure 2: (a) Streamlines in the radial-axial plane of the eigenfunction corresponding to $j = 1$, $k = 1$. (b) Plot of the largest eigenvalue corresponding to the eigenfunction with $j = 1$, $k = 1$, as a function of the Reynolds number. (c) Neutral stability boundaries for the system with and without symmetry constraints along y.

Application of the energy stability method, Doering and Gibbon (1995); Huang et al. (2015), to the fully constrained system results in a critical value of the Reynolds number

$$Re_E = 4\sqrt{2}, \tag{20}$$

below which the energy of every finite amplitude perturbation decreases monotonically, so the flow is globally stable. Interestingly, the stability boundary does not depend on the rotation number Ω, and coincides with the linear stability boundary (19) at $\Omega = 0.5$.

It is worth pointing out that, because of how symmetry constraints are defined, the constrained model problem can be seen as the axisymmetric flow arising between two solid parallel plates, with rotation described by the rotation number Ω, where the no-slip condition $u = v = 0$ and the free-slip condition $\partial w/\partial y = 0$ are imposed on $y = 0$ and $y = \pi$ From this standpoint, the unstable eigenmodes shown in figure 2-(a), can ideally represent the more common Taylor vortex structure confined between two parallel plates, with the boundary conditions specified above. Our stability results can be thus compared with the stability calculations of the rotating plane Couette flow (RPC), see for instance Lezius and Johnston (1976), Tsukahara et al. (2010). Within the definition

of nondimensional parameters defining the system adopted in this paper, linear stability analysis predicts for that case that longitudinal roll cells will develop if the Reynolds number is above the critical value:

$$Re_L = \frac{10.34}{\sqrt{\Omega(1-\Omega)}}, \tag{21}$$

which has a minimum of $Re = 20.7$ for $\Omega = 0.5$. Interestingly, this boundary has the same functional form of that for the system considered in this paper, given by equation (19), but the constant appearing in the equation is about 3.7 time larger. It may be argued that this result is mainly due to the damping effect of the no-slip condition on w for the classical RPC flow, which is relaxed by a weaker free-slip condition in the present case. This is in analogy with Rayleigh-Bènard convection, for which the critical Re is lowered by the adoption of free-slip boundary conditions on both the upper and lower boundaries of the domain, see Drazin and Reid (2004).

Linear stability analysis indicates that the present model flow is linearly stable at all Reynolds numbers at the two extreme values of the rotation number, i.e. 0 and 1. For values of Ω in the interval $[0, 1]$, the linear Couette flow is globally stable, i.e. stable to finite amplitude perturbation, if it is linearly stable, Ahmadi et al. (2015). This feature appears to reflect the experimental observations of the full three-dimensional Taylor-Couette problem, where results of linear stability analysis closely predict the appearance of the first bifurcation which develops into a set of toroidal vortices, as exemplified by the early work of Taylor (1923). More formally, such results has been proven by Joseph and Hung (1971) for the case of no-slip boundary conditions. For the present model with double-periodic boundary conditions, Huang et al. (2015) performed nonlinear stability analysis using a novel methodology based on sum-of-squares-of-polynomials optimisation techniques, extended from the work of Goulart and Chernyshenko (2012), and demonstrated that the flow is in fact stable to finite amplitude perturbations if it is linearly stable, in the range $\Omega = [0.2529, 0.7471]$.

A key point is that the full three dimensional plane Couette flow with no rotation, $\Omega = 0$, is not stable to finite amplitude perturbations at all Reynolds numbers, although it is with respect to infinitesimal perturbations. Studies by Nagata (1988, 1990) and Faisst and Eckhardt (2000) show that some of the nonlinear states appearing for the rotating case, e.g. the wavy vortex flow, survive the limit $\Omega \to 0$ and give rise to

finite amplitude solutions of plane Couette flow. In addition, experimental observations indicate that turbulent spots can become self-sustained from $Re = 360$, Tillmark and Alfredsson (1991); Daviaud et al. (1992); Prigent et al. (2002). Hence, the simple proof given here, also applicable to the case where no-slip conditions are enforced on the inner and outer walls, shows that these states and regimes must be three-dimensional as the flow is globally stable to axisymmetric perturbations.

4. Results

Numerical results of simulation of the system are reported in this section. Results are first presented for the fully constrained system in section 4.1, which shows a simpler dynamical behaviour than the partially constrained system, for which results are presented in 4.2. Because of the large parameter space that this system possesses, we reported results mainly for a rotation number $\Omega = 0.5$, which is the most unstable condition. As a consequence, the focus of the results section is on highlighting the relevant transitions that the model flow undergoes as the Reynolds number is increased.

4.1. Fully constrained system

For a given rotation number Ω, when the Reynolds number is moderately above the neutral stability boundary (19), unstable perturbations to the basic Couette flow grows exponentially in time until saturation and a steady state solution is eventually reached. For the TC flow, in the narrow gap limit and in the case of arbitrarily large domains along the axial coordinate, the most unstable bifurcating structure has a transverse wavelength of about 3.117, see Nagata (1986), and the vortex cells are confined into torii of almost square section. In the present case, the nonlinear steady flow results from the growth of the discrete wave number $j = 1, k = \pm 1$ and describes a pattern of four counter-rotating vortex cells on the domain $\mathscr{V}$, which have an exactly square cross-section, owing to the symmetry constraints imposed on the solution. The bifurcation is super-critical and no oscillatory behaviour is observed during the linear growth of the disturbances, as the imaginary part of the unstable eigenvalue is identically zero, Speziale and Wilson (1989).

Panel (a) of figure 3 shows time histories of the integral perturbation kinetic energy, defined as

$$K = \frac{1}{2} \int_{\mathscr{V}} \mathbf{u} \cdot \mathbf{u} \, \mathrm{d}\mathscr{V}, \tag{22}$$

for increasing values of the Reynolds number above the stability boundary for $\Omega = 0.5$. The curves are parametrized by the ratio $\eta = Re/Re_L$, up to a maximum value $Re = 3Re_L \approx 16.97$. The initial conditions for all these simulations was a flow field defined by small Gaussian random fluctuations of u and ψ, and such that $K(0) = 10^{-4}$.

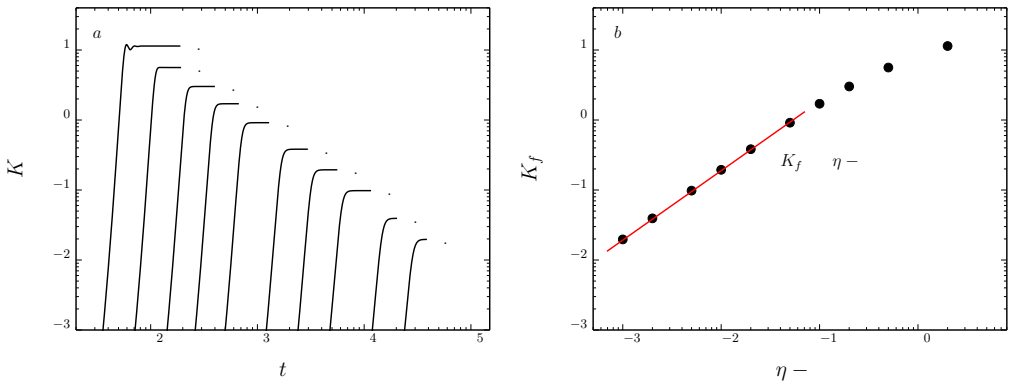

Figure 3: (a): Time histories of the perturbation kinetic energy for increasing value of the parameter $\eta = Re/Re_L$, indicated in the figure; (b) kinetic energy of the steady solution as a function of $\eta - 1$.

Although not visible from the figure, the time histories indicate a first initial decrease of the perturbation energy, associated with a rapid dissipation of high-wave-number components. A stage of exponential growth of the perturbation kinetic energy then follows, dominated by the growth of the unstable normal mode. As the perturbation amplitude becomes finite, the energy conserving nonlinearity of the governing equation feeds energy from the unstable, energy producing mode to the stable, dissipative high-wave numbers modes. Eventually, this results in the balance between these two components and a steady state solution is reached. In addition, just above the bifurcation the perturbation kinetic energy of the nonlinear final steady state k_f grows linearly with the Reynolds number, as shown in panel (b) of figure 3.

The increase in kinetic energy of the steady state solution is also associated with a drastic increase in the spectral richness, with high-wave number components contributing in larger part to the total energy. The changes that the energy spectrum of the steady solution undergoes are similar to those observed for the full Taylor-Couette problem, i.e. with curvature effects included, reported by Fasel and Booz (1984). As argued by these authors, this feature is due to the effect of the nonlinear term of the governing equations,

which cascades energy from the fundamental mode to wave numbers at higher harmonics, via triadic interactions.

In physical space, such a feature is mainly reflected as a distortion of the vortex pattern, with a sharp increase of the velocity gradients, especially close to the boundaries of the Taylor vortices. This behaviour is represented in figure 4, which shows the distribution of the azimuthal velocity component for three values of the Reynolds number, i.e. 10, 50 and 500, in panels (a), (b) and (c) respectively, for $\Omega = 0.5$. Note that because of the symmetries, the solution in the domain $\mathscr{V}^*$ only is shown. Also note that, for this particular case, the Taylor vortices reported rotate counter-clockwise. In panels (d),

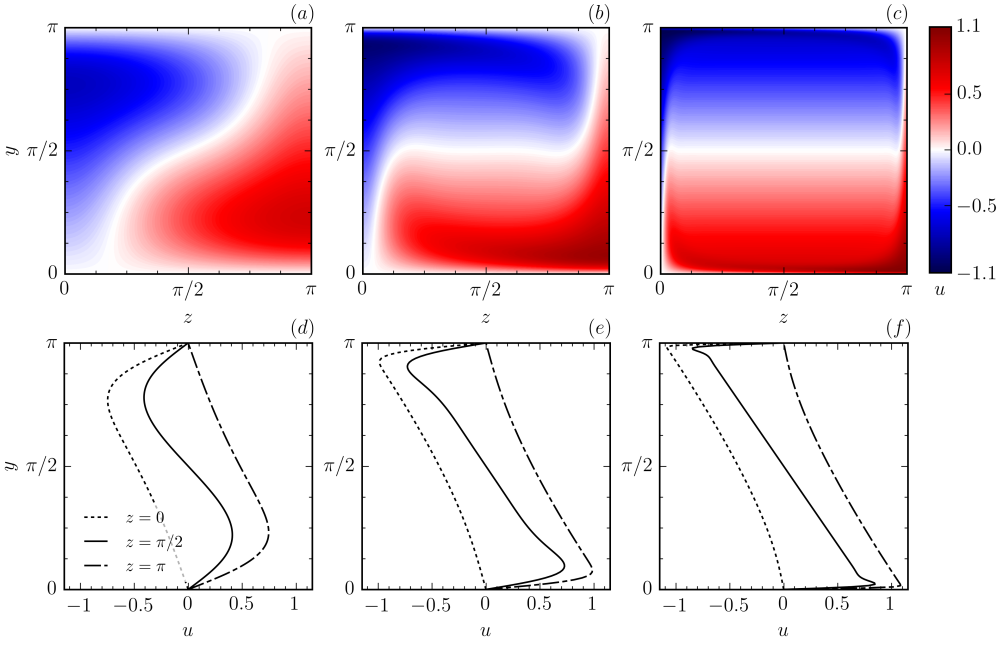

Figure 4: Top three panels: colour maps of the azimuthal velocity component for $Re = 10, 50$ and 500, at $\Omega = 0.5$. Bottom panels: profiles of u along y for three different z.

(e) and (f), profiles of u along y are reported for $z = 0, \pi/2$ and π, for the same three Reynolds numbers, respectively. We observe that as the Reynolds number increases, the distortion of the distribution of the azimuthal velocity u becomes stronger, induced by a stronger rotation of the secondary flow in the radial-axial plane. In particular, the positive/negative peak of u moves from $y = \pi/2$, as for the unstable eigenfunction of figure 2-(a), towards the lower/upper boundaries, producing a large increase in the magnitude

of the velocity gradient $\partial u/\partial y$ in these regions, where most of the dissipation of kinetic energy takes place. The thinning of these boundary layers is connected to the increase in the torque required to sustain the rotation of the two cylinders, as observed by Fasel and Booz (1984), which investigated axisymmetric laminar flow for the super-critical Taylor flow. However, in the current work no attempt at calculating torque scaling laws and distributions were performed.

The distortion of the Couette flow partially saturates, in the sense that the maximum value of the perturbation u reaches a maximum value of about 1.1, while the gradient $\partial u/\partial y$ at the upper and lower boundaries continues to increase with Re, as well as the circulation of the Taylor vortices and the associated vorticity levels.

We anticipate at this stage, but more details will be outlined in the rest of the paper, that for the flow model described in this paper we observed steady solutions of the nonlinear equations at relatively high Reynolds numbers, as for example the case at $Re = 500$ shown in panel (c) of figure 4. Extensive numerical simulations of the fully constrained system did not provide evidence of secondary instabilities of the vortex pattern described here. This feature appears in contrast to the behaviour that the full three-dimensional problem exhibits, both for the rotating plane Couette flow, see Nagata (1986), Tsukahara et al. (2010), and for the Taylor-Couette problem, Andereck et al. (1986), Jones (1982), Coles (1965), with curvature effects taken into account. In these cases, a large class of three-dimensional nonlinear solutions appearing in a secondary bifurcation has been found, in the form of rotating waves, exemplified by wavy vortex flow structure, after the work of Coles (1965). We argue that the presently-observed results arise from the particular symmetries applied to the flow. For example, the formation of previously-known three-dimensional states and regimes is clearly prevented by assuming axis-symmetric disturbances to the basic flow. Furthermore, application of symmetry constraints on the velocity components, in particular from the constraints in the z direction, results, as discussed above, in a reduced square domain. These results seem to highlight the importance of three-dimensional mechanisms and instabilities in producing and sustaining states observed in the three dimensional flow.

Figure 5 reports colour maps of the azimuthal vorticity for the three Reynolds numbers as in figure 4. Note that because of the specific boundary conditions and because

of the full symmetries imposed on the solution, the vorticity is zero on the boundary of the vortices. There are a few interesting features to observe. Firstly, as Re increases the vorticity field tends to a patch of constant vorticity surrounded by very thin boundary layers, where most of the variation takes place. This results appears in qualitative agreement with the theoretical model for the viscous flow between rotating cylinders in super-critical conditions, proposed by Batchelor, see Donnelly and Simon (1960). In this model, which provides scaling laws for the viscous torque and for other quantities, the flow is assumed to be composed of rotational core regions where viscous dissipation is negligible, surrounded by thin layers where viscous forces are relevant. A second feature

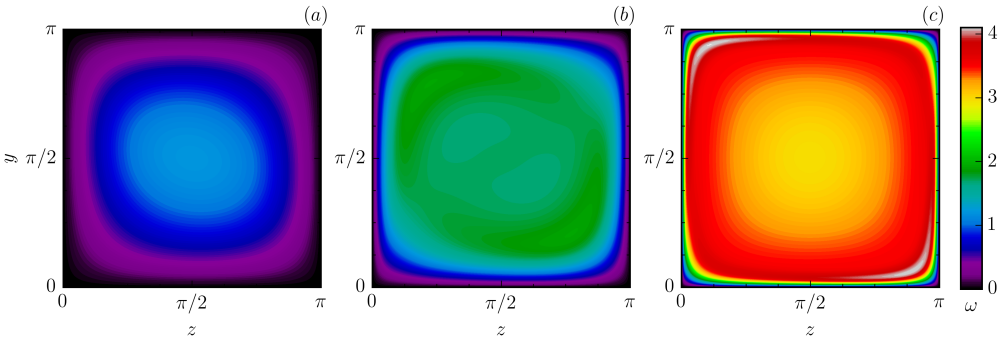

Figure 5: Colour maps of the azimuthal vorticity component for $Re = 10, 50$ and 500, at $\Omega = 0.5$.

is the fact that the magnitude of the azimuthal vorticity, and the associated velocities in the axial-radial plane, increase with the Reynolds number, while, as anticipated, the u component of the nonlinear perturbation reaches a constant maximum value.

Results not reported here for the sake of brevity, regarding the effect of the variation of the rotation parameter, indicate that the effect of varying Ω from 0.5 is analogous to a reduction of the Reynolds number and that if a too small or too large value of the rotation number is chosen, such that the Couette flow is linearly stable, the steady Navier-Stokes solver produces a solution decaying exponentially to zero.

It is worth noting that other stable steady solutions have been observed for the fully constrained system, other than the solution with toroidal vortices with square cross-section. For instance, by seeding the initial condition with a finite amplitude perturbation at a single wave number $j = 1, k = n$, it is possible to obtain by numerical integration

steady states with a larger number of vortices, precisely $4n$, confined in torii elongated along the radial direction, having rectangular cross-section, with width π/n and height π. However, numerical results appears to indicate that these steady solutions have a basin of attraction of limited size and a too large perturbation is sufficient to bring the system towards the state with four square-cross-section vortices. In addition, these nonlinear states are also linearly unstable for some value of the Reynolds number.

A typical transient solution of the flow, started from small amplitude random perturbations of the Couette flow, exhibits a wide range of complex flow features. An example is shown in figure 6 which reports the time history of the perturbation kinetic energy for the fully constrained system, at $Re = 500$ and $\Omega = 0.5$. On top of the time history, eight black dots denote time instants where a snapshot of the flow was extracted, which have been then represented in the eight panels of figure 7, showing colour maps of the azimuthal velocity. In addition, the plots report a few selected contour lines of the streamfunction, which also denote streamlines of the flow in the radial-axial plane. Dashed contours indicate negative values of ψ. In panel (a), we observe a pattern of elongated vertical streaks of velocity, originated by the linear growth of the most unstable eigenfunction of the Couette flow, which for this Reynolds number, has $k = 3$, which would give rise to three elongated vortices along the radial direction y. We note at this stage, that the way the results of this simulation have been obtained have no experimental counterpart, since typically in experimental circumstances the velocities of the cylinders are started from zero and are increased up to the desired value, which produces a well defined sequence of bifurcations and flow patterns. The Taylor-Couette flow is known to be very sensitive to the experimental procedure, as demonstrated in the work of Coles (1965), which revealed a very complex set of flow regimes whose existence did not depend only on the precise point in parameter space, but also on the trajectory in parameter space that was taken to reach the desired state.

The transient growth of the amplitude of the unstable mode eventually saturates due to nonlinear effects, which result in the development of "puffs" of relative high/low azimuthal velocity, panel (b), that are accelerated down/up by the action of the Coriolis force. The following turbulent motion, panel (c) to (g), is characterised by the competition between several vortical structures of relatively large size, which merge together and

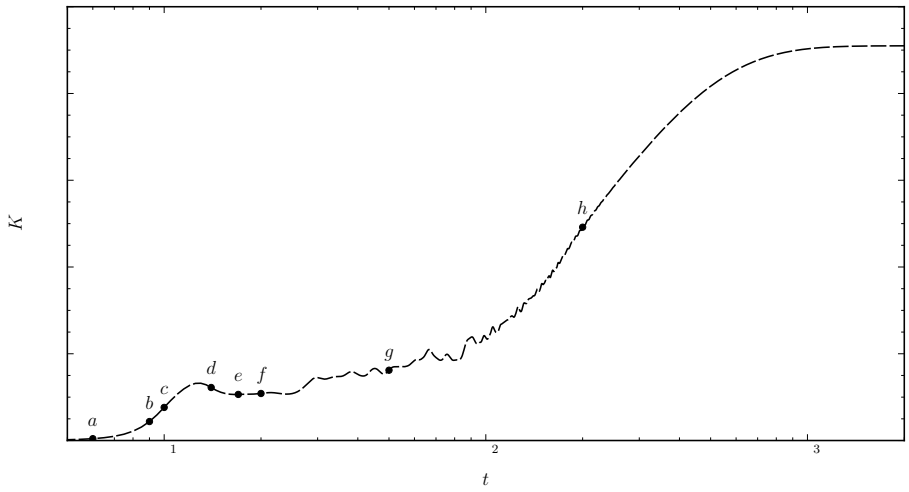

Figure 6: Time history of the perturbation kinetic energy for $Re = 500$ and $\Omega = 0.5$. The black dots refer to the instants in time for which the snapshots reported in figure 7 were extracted.

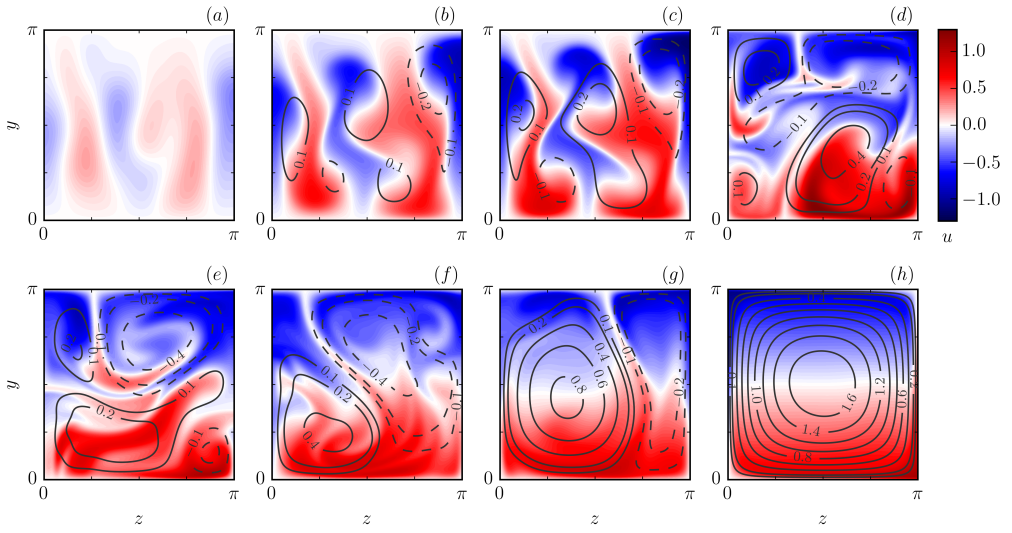

Figure 7: Snapshots of the flow transient at $Re = 500$ and $\Omega = 0.5$, corresponding to the black dots in figure 6. Colour maps denote the azimuthal velocity component, from dark red, $u = 1.1$, to dark blue, $u = -1.1$. Selected contour lines of the streamfunction ψ are also reported to highlight the pattern of streamlines. A movie is available online.

produce, eventually a single large steady structure, panel (h), whose circulation increases asymptotically to the final value. Interestingly, as anticipated, this flow pattern appears stable at higher Reynolds numbers, as simulations at $Re = 2000$ pointed out.

During the transient, ejections of fluid with high/low azimuthal velocity are observed from the upper/lower boundaries, which develop into mushroom-like flow patterns that are eventually dissipated. An example can be observed in panel (f), where an ejection of low speed fluid is observed from $y = 0, z = \pi/2$ upwards. These structures are typically originated at the boundary, by the effect of two counter-rotating longitudinal vortices, which produce such streaks of high or low velocity, associated with streaks of the azimuthal vorticity. Interestingly, they appear of the same family of flow patterns observed in high-Reynolds number simulations of the turbulent three-dimensional Taylor-Couette flow, for example in the work of Dong (2008), Brauckmann and Eckhardt (2013). The latter authors point out that, in analogy with thermal convection, Eckhardt et al. (2007), these structures correspond to thermal plumes observed in Rayleigh-Bènard flow, to which the Taylor-Couette flow also share the same structural instability features, as discussed by Lezius and Johnston (1976). In Rayleigh-Bènard flow, the transported quantity is the temperature Θ, with the time and space averaged thermal flux $\langle v\Theta\rangle_{A,t} - \kappa\partial_y\langle\Theta\rangle_{A,t}$ conserved along the gap, where v is the vertical velocity, κ is the thermal conductivity, and the spatial average is performed over an horizontal plane. On the other hand, it is well known, see Bech and Andersson (1996) and Ostilla-Mónico et al. (2013), that in the rotating plane Couette flow, RPC, and in the TC flow in the narrow gap limit, the transported quantity is the x momentum u, so that the flux $\langle vu\rangle_{A,t} - \nu\partial_y\langle u\rangle_{A,t}$ is conserved along the gap width, where ν is the kinematic viscosity of the fluid.

4.1.1. Stability of Taylor vortices

It has been shown that the solution in a typical transient of the fully constrained system eventually settles down to a steady state, with Taylor vortices having square cross-section. In this section we present numerical calculations of the linear stability analysis of these Taylor vortices at increasing Reynolds numbers.

As for the analytic stability calculations of the Couette flow, we use the azimuthal velocity-streamfunction formulation, which eliminates the pressure from the governing equations and simplifies the numerical set up. We consider a decomposition of the so-

lution as the sum of the Taylor vortices flow, (u^0, ψ^0), over which the infinitesimal perturbations (u, ψ) can develop. Assuming that the solution of this initial-value problem is a linear combination of normal modes, of the form $(u, \psi) = (\tilde{u}, \tilde{\psi})e^{\lambda t}$, and substituting this functional form into the linearized governing equations leads to the generalised differential eigenvalue problem:

$$\lambda\tilde{u} = -\frac{\partial\tilde{\psi}}{\partial z}\frac{\partial u^0}{\partial y} + \frac{\partial\tilde{\psi}}{\partial y}\frac{\partial u^0}{\partial z} - \frac{\partial\psi^0}{\partial z}\frac{\partial\tilde{u}}{\partial y} + \frac{\partial\psi^0}{\partial y}\frac{\partial\tilde{u}}{\partial z} + \Omega\frac{\partial\tilde{\psi}}{\partial z} + \frac{1}{Re}\nabla^2\tilde{u} \tag{23}$$

and

$$\lambda\nabla^2\tilde{\psi} = -\frac{\partial\tilde{\psi}}{\partial z}\frac{\partial}{\partial y}(\nabla^2\psi_0) + \frac{\partial\tilde{\psi}}{\partial y}\frac{\partial}{\partial z}(\nabla^2\psi_0) - \frac{\partial\psi_0}{\partial z}\frac{\partial}{\partial y}(\nabla^2\tilde{\psi}) + \frac{\partial\psi_0}{\partial y}\frac{\partial}{\partial z}(\nabla^2\tilde{\psi}) - \Omega\frac{\partial\tilde{u}}{\partial z} + \frac{1}{Re}\nabla^4\tilde{\psi} \tag{24}$$

or in a compact, symbolic form:

$$\lambda\mathscr{B}(\mathscr{X}) = \mathscr{A}(\mathscr{X}) \tag{25}$$

where $\mathscr{B}$ and $\mathscr{A}$ are linear differential operators and $\lambda, \mathscr{X}$ are the eigenvalues and the eigensolutions of the problem, which need to satisfy the full symmetry constraints (8, 9).

The differential problem of equation (25) is spatially discretized on a uniform grid using second order accurate centred finite differences, covering only the reduced domain $\mathscr{V}^*$, with the appropriate discretized boundary conditions. Because the Taylor vortex flow (u^0, ψ^0) contributes as a set of known constant coefficients in (23, 24) a steady Navier-Stokes solver, based on a second order finite difference discretization of the governing equations, equations (6) and (7), and using a successive over-relaxation method, Smith (1985), was developed to quickly find the steady state solution (u^0, ψ^0). The resulting sparse generalised eigenvalue problem was then solved with the ARPACK[1] libraries using the Implicitly Restarted Arnoldi Method, usually solving for the first k eigenvalues with the largest real part.

The eigenvalue problem solver was validated with the the eigenvalue spectrum obtained via Dynamic Mode Decomposition, (DMD), see Schmid (2010). DMD is a linear data-based technique, operating on snapshots of a simulation, that can recover part of the spectrum of the linear operator underlying the temporal sequence of the snapshots.

[1] http://www.caam.rice.edu/software/ARPACK/

For this task, a sequence of snapshots was first obtained from a nonlinear numerical simulations of the perturbed dynamics of the flow evolving in a very small neighbourhood around the steady state, obtained as a spectrally accurate steady solution. DMD was then applied on a sequence of snapshots describing the transient towards the steady state. Tests were conducted at different Reynolds and rotation numbers and indicated a very good agreement of the results of the two approaches, typically well below 1% for the leading eigenvalue, which dominates the transient.

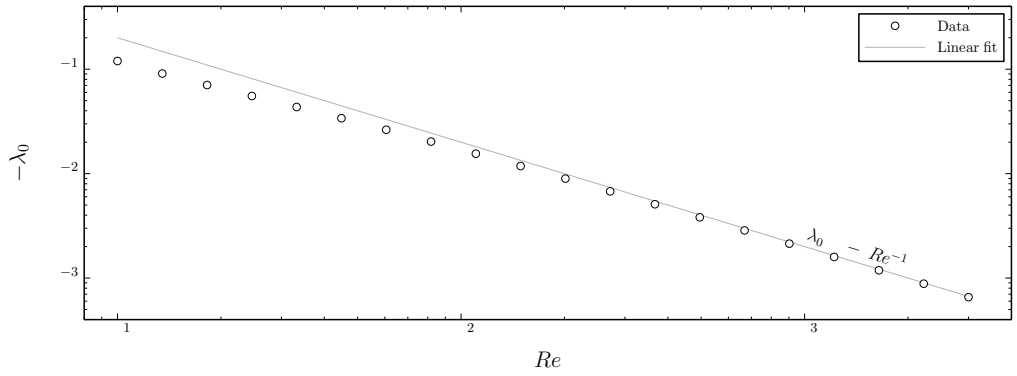

Figure 8: Leading eigenvalue of the linear stability problem, as a function of the Reynolds number, for $\Omega = 0.5$. The sign of the eigenvalue has been inverted to allow plotting of the data on the bi-logarithmic scale.

Figure 8, shows the behaviour of the real part of the leading eigenvalue λ_0, the one with the largest real part, as a function of the Reynolds number, for a rotation number Ω equal to 0.5. The data points were obtained using a resolution of five hundred grid points along the two coordinates, which is sufficiently high to reach convergence of the results at all the Reynolds numbers reported in the figure to within an accuracy indistinguishable from the graph. For the sake of clarity, in the plot we inverted the sign of the eigenvalue since we reported the data on a bi-logarithmic scale, to emphasise the power law that describes the data. The plot clearly indicates that the leading eigenvalue, which is purely real, grows as $-c/Re$ where c is a positive real constant close to 2, obtained by a least squares fit of a line on the three last data points. Therefore, the real part of leading eigenvalue never becomes positive, indicating that for the specific model problem considered and with the full symmetries imposed, the Taylor vortices are linearly stable at all Reynolds numbers, even though their spatial structure changes with Re. This is

in stark contrast to what observed for the three dimensional RPC and TC flows. It may be argued that this results is intrinsically due to the assumption that the perturbations which are allowed to grow on the steady state have to be azimuthal. This constraint appears to prevent the growth of instabilities on the thin layers of strong shear that grow on the boundaries of the Taylor vortices and that in the full three-dimensional problem give rise to a secondary bifurcation, which results in the time dependent, intrinsically non-azimuthal wavy vortex flow structure, as reported by Nagata (1986).

4.2. Partially constrained system

The partially constrained system displays a wider range of behaviour and shows fundamental differences with respect to the fully constrained condition. We first present results of linear stability analysis of the secondary flow arising after the first bifurcation, in section 4.2.1, and we then discuss the peculiar transitional behaviour of this case, in section 4.2.2.

4.2.1. Stability of Taylor vortices

Due to the symmetries along the radial direction only, for the partially constrained system the generalised differential eigenvalue problem (25) is solved only on the lower half of the full domain, in $\tilde{\mathscr{V}}$.

The stability of the steady solution with four Taylor vortices with square cross section, presented in the previous section for the fully constrained system, is discussed first. Solution of the eigenvalue problem yields a set of eigenfunctions which can be cast in two separate classes. For both classes, the eigenfunction satisfy the constraints of the problem along y. In addition, eigenfunctions of the first class have u/ψ even/odd along z, while eigenfunctions of the second class have u/ψ odd/even along z. The eigenfunctions of the first class are the same of the fully constrained system. Therefore, the partially constrained system has the same eigenfunctions of the fully constrained problem, and these were shown to be stable at all Reynolds numbers, plus a set of other eigenfunctions.

An interesting feature is that one of the eigenfunctions of the second class possesses an eigenvalue which, within discretization errors, is identically zero. This behaviour is associated to the fact that generalised differential eigenvalue problem of equation (25) admits a non trivial solution $\mathscr{X}^*$ such that:

$$\mathscr{A}(\mathscr{X}^*) = 0 \tag{26}$$

or, equivalently, that the linearized disturbance equations (23) and (24) admit a steady solution. This was verified numerically, by solving iteratively, using a biconjugate gradient method, the linear system $\mathbf{Ax} = 0$ resulting from the discretization of equation (26). Depending on the initial guess, the solution $\mathbf{x}$ converged to either the trivial solution or to the eigenfunction with zero eigenvalue obtained by solution of the full eigenvalue problem.

The physical meaning of this null eigenvalue is determined by the assumption of periodic boundary conditions along the axial direction, rather than by the symmetries of the problem. In fact, the corresponding eigenfunction, which we will refer to as the "shift mode" represents spatially a neutrally stable axial displacement of the base solution. Ideally, adding this perturbation to the steady state solution does not change its spatial structures, nor its energy, but it only displaces the vortices along z proportionally to the perturbation amplitude. We argue that such a feature is due to the particular boundary condition imposed for w at the lower and upper boundaries which reduces to the free-slip condition $\partial w/\partial y = 0$ at these two boundaries, so that any perturbation that shifts the Taylor vortices along z does not produce a dissipation nor a increase of energy. In the case of no-slip boundary conditions, the occurrence of a null eigenvalue has not been reported in the relevant literature. Such behaviour was verified in numerical simulations, which were started by perturbing the steady solution with the shift mode with increasing amplitudes. After a small transient the flow returned to a steady state, shifted along z by an amount proportional to the perturbation amplitude. The small transient observed is likely due to the fact that finite perturbations were added to the steady solution, which introduced a slight deformation of the nonlinear vortex structure.

In figure 9 colour maps of the shift mode for four increasing values of the Reynolds number are reported. These were obtained with well resolved computations of the steady solution with a grid size of 500×1000 grid points in the axial and radial directions. Colours range from dark blue to dark red, for values of u from 1 to -1. The maps also show nine equally spaced contour lines of the streamfunction, from -0.8 to 0.8, in steps of 0.2, with dashed lines indicating negative values of ψ. Note that, the solution is reported on the rectangle $[0, \pi] \times [0, \pi]$ only, because of the symmetry properties of the eigenfunction along z, where $u(\pi + z, y) = -u(\pi - z, y)$ and $\psi(\pi + z, y) = \psi(\pi - z, y)$.

For plotting purposes, the amplitude of the eigenfunctions has been arbitrarily scaled such that both u and ψ have maximum value equal to one, but the ratio between the maxima of these two quantities changes with the Reynolds number, from 0.75, at the lower Reynolds number reported, to 1.74, for the largest. In each panel of the figure,

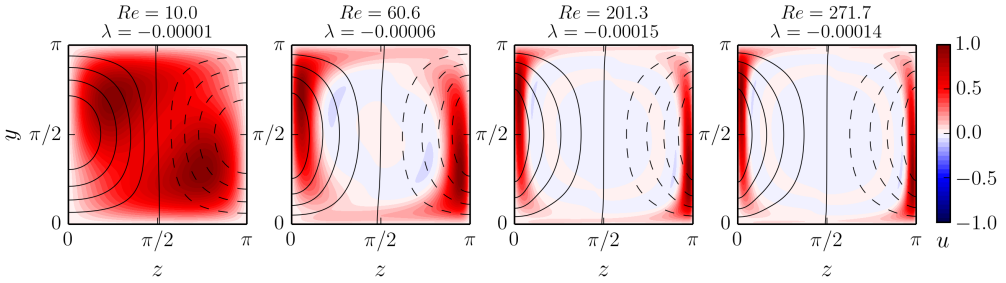

Figure 9: Eigenfunctions of the eigenvalue problem for the partially constrained system that have a null eigenvalue, for four increasing values of the Reynolds number. The colour maps refer to the azimuthal velocity component. Selected contour lines of the streamfunction are also reported, (negative dashed).

the title reports the Reynolds number and the corresponding eigenvalue, which should be identically zero. The observed deviation from the null value indicates essentially the accuracy of the stability calculations. As the Reynolds number increases, the shift mode displays larger gradients of the velocity along the two lateral boundaries, accordingly to the large gradients of the flow variables exhibited by the steady solution in these regions. This is because this eigenfunction describes a translation of the base flow and varies with the Reynolds number in order to accommodate the variations of the steady solution itself.

For the other eigenfunctions of the second class, the eigenvalues cross the real axis and become unstable for some critical Reynolds number. Interestingly, the growth of these instabilities is prevented in the fully constrained system because the corresponding eigenfunction would break the symmetries along z. Hence, it might be possible to draw more connections between the stability results of the partially constrained system and the original three-dimensional problem, for which a secondary bifurcation leads to nonlinear tertiary states. In figure 10 we show the behaviour of λ_0, the first eigenvalue whose real part becomes positive, for a few values of the Reynolds number around the transition point. Panel (a) shows the real part of the eigenvalue, whereas the imaginary part is reported in panel (b). Note that because of the very low magnitude of this eigenvalue,

both real and imaginary part have been scaled by a factor of one hundred.

The results were obtained by computation on a fine grid of 1000×500 points along the radial and axial directions, which was sufficient to achieve an accuracy of the estimated eigenvalue for at least two significant digits. The crossing point takes place at around $Re = 220$, based on polynomial interpolation of the four neighbouring data points. At

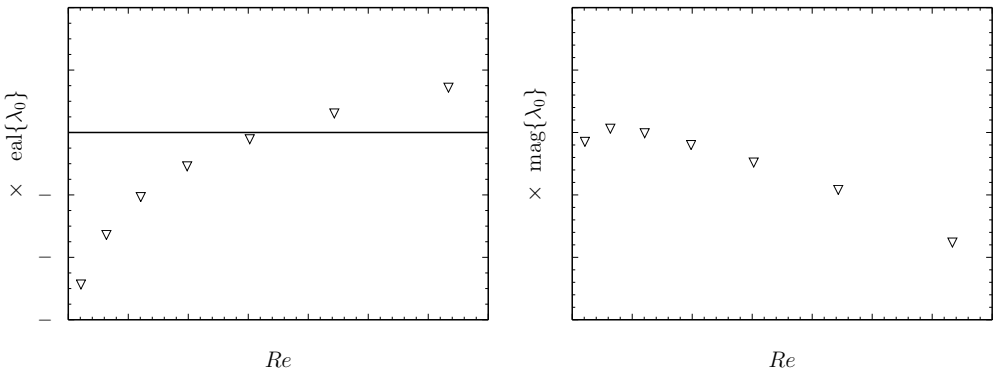

Figure 10: Real, (a), and imaginary, (b), parts of the eigenvalue which first crosses the real axis, as a function of the Reynolds number.

the crossing point, the value of the imaginary part of the eigenvalue is quite small, and it is of the order of 0.025. The system exhibits in general, and in particular at the onset of the instability relatively slow dynamics with very low growth or decay rates of the energy of the perturbation, as observed by the very low values of the real part across the entire range of Reynolds number reported in figure 10-(a).

The spatial structure of the corresponding eigenfunction is shown in figure 11. Colour maps of the azimuthal velocity u are reported for four increasing values of the Reynolds number, with colours ranging from dark red, $u = 1$, to dark blue $u = -1$. On the same plots, selected contours of the streamfunction are also reported for $\psi = \{0.2, 0.4, 0.6, 0.8\}$. Note that, for plotting purposes the eigenfunction have been normalised as for figure 9. As before, above each panel, the title indicate the Reynolds number and the real part of the corresponding eigenvalue. As it will be discussed in detail later, but it is anticipated here for the sake of completeness, in numerical simulations of the system the oscillatory growth of such eigenfunction corresponds to a periodic alternated contraction-expansion of the axial size of the two vortices, with one of them accommodating the variation of

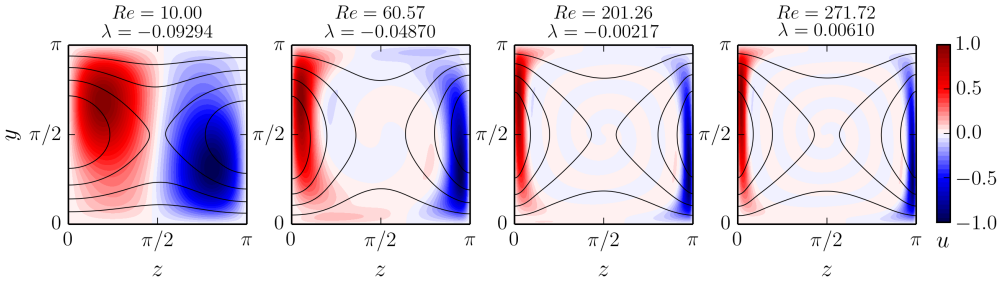

Figure 11: Variation with the Reynolds number of the first eigenfunction to become unstable. Colour maps refer to the azimuthal velocity component. Selected contour lines of the streamfunction are also reported.

the other.

4.2.2. Transitional behaviour and chaotic motion

The partially constrained system has a transitional behaviour that is significantly different to that of the fully constrained system. The simulation results displayed in figure 12 were obtained for unstable conditions at $Re = 250$ and $\Omega = 0.5$. In panel (a) the time history of the perturbation kinetic energy K around the point in time where abrupt transition takes place is reported. The two vertical segments denote the time interval for the detail reported in panel (b), where the vertical axis shows the energy of the perturbation around the steady state, which has energy K_s. The open circle in the same panel denotes the position in time of the snapshot reported in panel (c). Here the colour map refers to the azimuthal component u and ranges uniformly from -1 to 1, from dark blue to dark red. Selected contour lines of the streamfunction ψ are also reported. The initial condition for this simulation was obtained by perturbing the steady Taylor vortices with a small random perturbation. On the other hand, the steady state was calculated by running until convergence a simulation of the fully constrained system, for which the Taylor vortices are always stable. In panels (a) and (b) we observe that, in the first stages of the simulation, for $t \lesssim 2300$, the energy of the most unstable mode grows with a very slow rate and with very low dynamics, as it has been previously pointed out while discussing the results of the solution of the eigenvalue problem. The detail of the last stages of this growth shows a very small variation of the perturbation kinetic energy, despite the intense distortion of the structure of the flow, as visible in

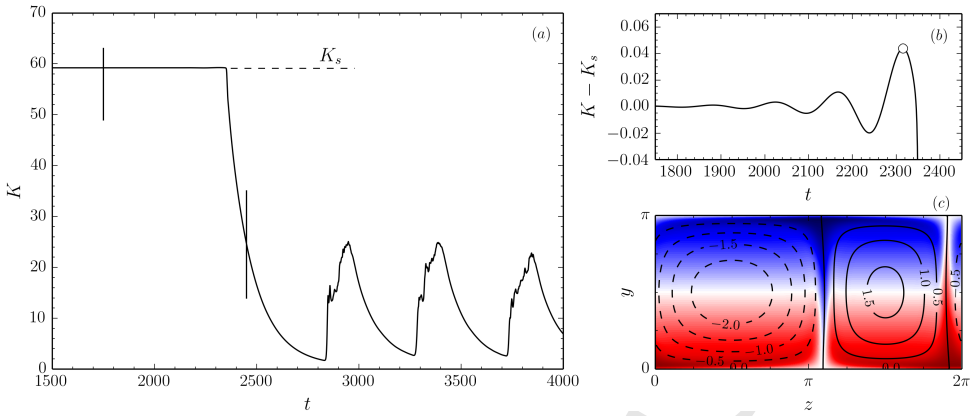

Figure 12: Simulation results for an unstable condition at $Re = 250$ and $\Omega = 0.5$. See text for description of the three panels.

the snapshot reported in panel (c), taken a few instants before the total collapse of the solution. We observe in the snapshot of panel (c) that the oscillatory growth of the unstable mode produces an alternating variation in the axial size of the vortices with the axial expansion of one vortex accompanied by a contraction of the other. The abrupt changes in the structure of the flow, that can be deduced from the strong decay of the kinetic energy after $t \approx 2300$ and in the following evolution, is related to the situation where one of the two vortices has shrunk to such a small size that the other vortical structure has become so large to occupy the entire domain. The following evolution of the flow is strongly chaotic and non periodic, as suggested by the time history of K for $t \gtrsim 2900$, which shows a long-period temporal pattern, a common feature of the flow for the partially constrained system.

Despite the fact that the solution with Taylor vortices is linearly stable for $Re \lesssim 220$, numerical simulations of the system at sub-critical values of Re appear to indicate that the corresponding fixed point has a basin of attraction of limited size and that the Taylor vortices are only conditionally stable. If the Taylor vortices are perturbed with a too large disturbance, the solution escapes from the fixed point and enters into the same chaotic attractor which has been shown previously for super-critical conditions in figure 12. It is worth pointing out that the secondary bifurcation of the full-three dimensional problem leads to tertiary states, time-dependent and time-independent, that are entirely three-dimensional, Nagata (1988). In addition, the bifurcations leading to these states

are all supercritical, whereas the presently observed bifurcation is sub-critical.

In figure 13 time histories of the perturbation kinetic energy for simulations of the partially constrained system at $Re = 200$, $\Omega = 0.5$ are reported. The initial condition for these simulations is the steady state solution plus a perturbation, which is taken as the most unstable eigenfunction multiplied by an appropriate coefficient, such that the perturbation energy is a fraction equal to a_0^2 of the steady state energy. Panels (a) and (b) shows the time histories for simulations with perturbation amplitudes $a_0 = 0.1$ and 0.2, respectively, while panel (c) shows a detail of the same time histories in the first stages of the simulations. Considering panel (c), we first observe that the two solutions

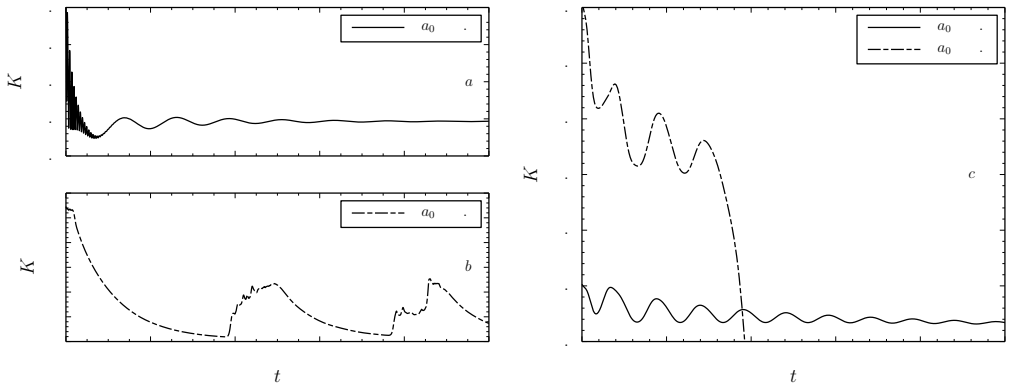

Figure 13: Panels (a) and (b) show time histories of the perturbation kinetic energy for two simulations with different initial conditions, with different amplitude a_0 of the disturbance added to the steady state solution. Panel (c) shows a detail of the same data for $0 < t < 50$. $Re = 200$, $\Omega = 0.5$.

display an initial transient with relatively fast dynamics, with a period of about six nondimensional time units. For both cases, this oscillation is due to the quick decay of some higher wave number components introduced together with the most unstable eigenfunction, because such an eigenfunction is computed by a finite difference solution of the eigenvalue problem which contains discretization errors.

For the lower amplitude this initial transient lasts up to about $t = 100$, as visible in figure 13-(a), after which the flow is dominated by the slow dynamics of the least stable eigenmode, described previously. On the other hand, for the larger amplitude, at $t \approx 15$, the system quickly exits from the neighbourhood of the Taylor vortices solution and evolves towards a chaotic solution, as visible in the time history of panel (b). This

event is associated with a rapid decrease of the kinetic energy, due to the strong increase of the viscous dissipation as the flow pattern breaks down into small scale structures, similarly to what is observed in super-critical conditions in the results of simulations of figure 12. Subsequently, the flow shows sustained chaotic behaviour, in which it can remain for indefinitely long times.

A set of simulations were run in order to roughly estimate the Reynolds number above which the preferred flow state is turbulent. A representative subset of the available results is shown in figure 14, which report time histories of the perturbation kinetic energy as a function of time, for four increasing values of the Reynolds number, i.e. 25, 50, 100, 150, in panels (a) , (b), (c) and (d), respectively. All these simulations were started by

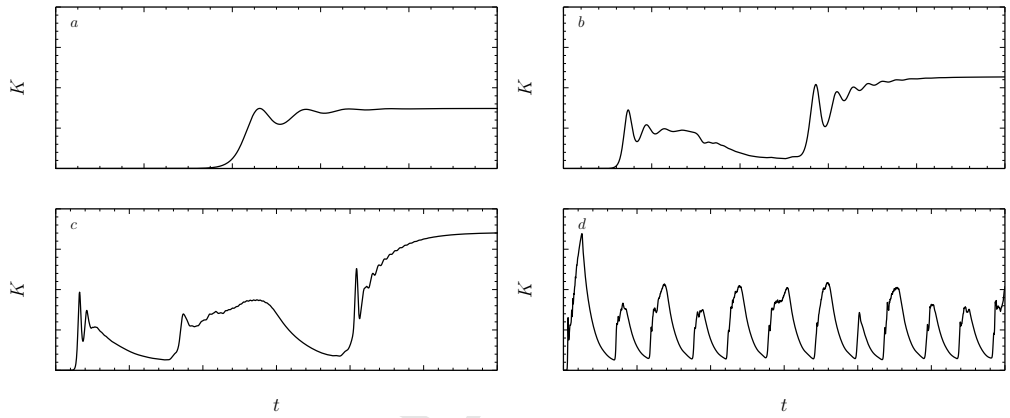

Figure 14: Time histories of the perturbation kinetic energy for simulations of the partially constrained system at $Re = 25,\ 50,\ 100$ and 150, in panels (a), (b), (c) and (d), respectively.

seeding the Couette flow with a small random perturbation of the flow variables.

In practice, in the initial stages of the simulations, the growth of the most unstable eigenmode of the Couette flow dominates the transient. For $Re = 25$ the most unstable eigenmode has $j = |k| = 1$, while for the other three cases shows the unstable mode has $j = 1$, $|k| = 2$. For $Re = 25$, the nonlinear saturation of the growth of the unstable mode produce a steady solution with four Taylor vortices in the entire domain $\mathscr{V}$, with square cross-section. This low value of the Reynolds number is such that the initial condition, close to $u = \psi = 0$, lies in the basin of attraction of the Taylor vortices solution, which is eventually reached with a relatively simple evolution. For the two higher Reynolds numbers, $Re = 50$ and 100, the transient is more complex. Careful observation of

animated sequences of the flow for these two values reveals that the growth of the mode with $|k| = 2$ does not saturate into a steady solution with eight rectangular vortices, but quickly becomes unstable and breaks up into a turbulent motion. The following transient is followed by a motion whose orbit appears to pass close to the four vortices solution, which is eventually reached after $t \gtrsim 150$ for $Re = 50$, figure 14-(b). On the other hand, for the higher Reynolds number, $Re = 100$, figure 14-(c), it takes longer for the flow to eventually reach the steady state. For this case, between $150 < t < 400$, the flow reaches a solution close to the steady state, but it breaks up at around $t \approx 300$.

Similar behaviour, where the flow state eventually settles to a steady state with four vortices with square cross-section could be observed up to a Reynolds number about 120, beyond which the system never reached a steady solution, at least for what could be deduced from running simulations for very long times, of about 10000 nondimensional time units. By contrast the flow remained in the sustained chaotic state introduced above. Such state is visible in the time history of the perturbation kinetic energy at $Re = 150$, figure 14-(d), and it can be observed that the motion remains chaotic over a relatively long period, with a characteristic time pattern made up of alternated instants of high-energy turbulent motion, followed by quasi-exponential smooth decays of K.

In order to shed light on the properties of these chaotic solutions, we report in the topmost panel of figure 15 the same time history of the perturbation kinetic energy at $Re = 150$, $\Omega = 0.5$, in light grey, together with the time histories of the perturbation kinetic energies $\tilde{K}_{u_i}$ associated with each of the three velocity components, $i = 1, 2, 3$. In addition, the lower six panels from (a) to (f), show snapshots of the flow taken at selected times, indicated as black dots on the time history of the perturbation kinetic energy in the top panel. The snapshots show the azimuthal velocity u, with colour maps ranging from -1, dark blue, to 1, dark red. Streamfunction contour lines are also shown. As anticipated, in the early stages of the simulation, $t < 30$, the growth of the eigenmode with eight vortices dominates the transient from the initial linear stages, up to the full nonlinear regime. This structure quickly breaks down, and the flow evolves into a pattern with four vortices, snapshot (a). Their axial size varies in time, until this pattern breaks down, shortly after snapshot (b), originating a fast axial motion, snapshot (c). This event is followed by a long transient decay of energy, from $t \approx 130$ to $t \approx 350$, where the

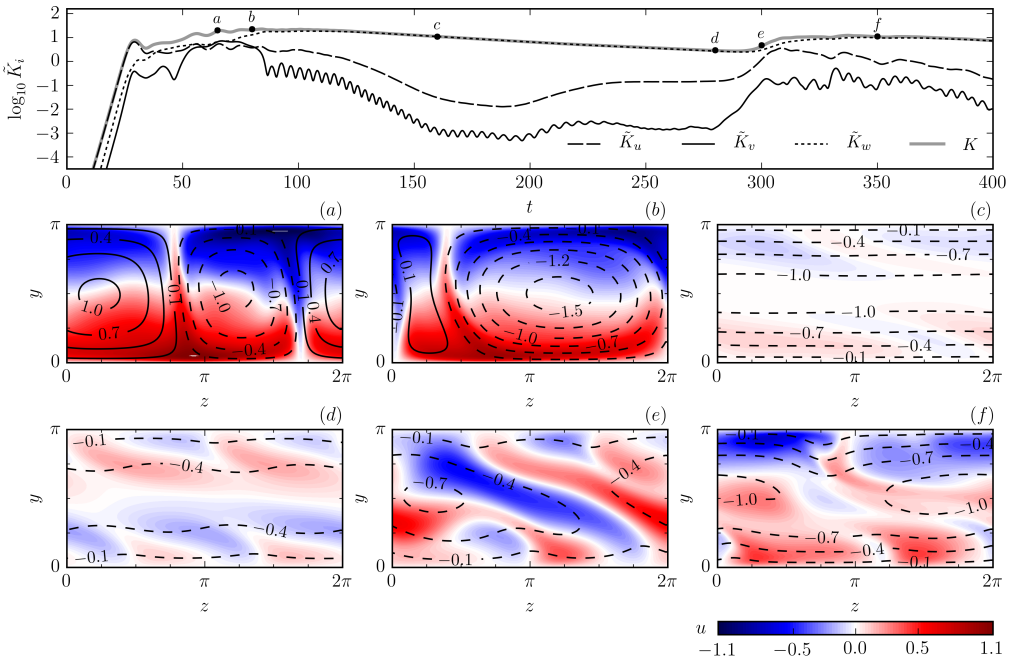

Figure 15: Top panel: time history of the perturbation kinetic energy K for a simulation of the partially constrained system at $Re = 150$, $\Omega = 0.5$, reported as a light grey thick line. In the same panel the other three curves denote the fraction of energy associated with each velocity component. Panels from (a) to (f) show snapshots of the flow at the time instants indicated in the top panel by black dots. The snapshots report colour maps of the azimuthal velocity and selected contours of the streamfunction. A movie of the sequence is available online.

intensity of the axial motion decays quasi-exponentially. This axial flow can be described as $w \approx Ccos(y)$, where C is a coefficient of decaying amplitude, and a stronger shear component $\partial w/\partial y$ is observed in the middle of the domain at $y = \pi/2$. In the central part of the transient, when the contributions of the azimuthal and radial components is small, the kinetic energy of the axial motion decays as $e^{-2t/Re}$, as expected by a pure decay by diffusion of the axial motion. The time series of $\tilde{K}_{u_i}$ in the top panel clearly indicate that the axial motion contributes almost exclusively to the total energy of the perturbation. A peculiar feature of this transient decay is the appearance of a low energy disturbance of the axial flow, travelling on top of it along the axial direction and clearly observable in snapshot (d). Travelling wave solutions do indeed exists for rotating plane Couette flow, Marcus (1984); Andereck et al. (1986); King et al. (1984) but they travel along the azimuthal direction and not axially. Hence, it appears that the presently observed regime

might be a unique feature of the model flow. We observe that the energy associated with such disturbance is very weak compared to the energy of the axial flow. Eventually, this axial flow appears to become unstable, and produces a fast growth of the perturbation kinetic energy as it breaks down, snapshot (e). In the interval between snapshots (e) and (f), the chaotic motion often resembles the four vortex solution but if the Reynolds number is high enough, a steady state is never reached and the pattern described here repeats for indefinite times.

The spatial structure of the disturbance associated to the travelling wave along the transient decays is shown in figure 16-(b), which reports a snapshot of the flow evolution taken at $t^* = 260$. The figure shows the colour maps of the azimuthal velocity perturbation u. In addition, to describe the structure of the travelling wave, we have reported the contour lines of the perturbation of the streamfunction, defined as

$$\psi'(z, y, t^*) = \psi(z, y, t^*) - \psi^0(y, t^*), \tag{27}$$

where

$$\psi^0(y, t^*) = \frac{1}{2\pi} \int_0^{2\pi} \psi(z, y, t^*) \mathrm{d}z. \tag{28}$$

The quantity ψ' represents the local fluctuation with respect to the "mean" component ψ^0. Due to the strong prevalence of the axial component, this "mean" component depends on y only and it is calculated by taking the spatial average of the streamfunction along lines at constant y. This mean component is shown in panel (a) of the same figure, where $w^0 = -\partial\psi^0/\partial y$ is shown. Intuitively, this quantity is the fluctuation over the mean axial flow and the choice of the spatial average is justified by its relatively slow decay. Note that in figure 16, the contour labels indicate the value of $100\psi'$, because of the relatively low value of ψ'.

We first observe that, at this Reynolds number, the spatial structure of the travelling wave is periodic in z with wavelength approximately equal to π. The second observation is that the disturbance is confined in a region close to the upper and lower boundaries, with a similar, but reversed, structure on the two sides. This appears to be due to the fact that the mean axial flow has opposite sign on the upper and lower regions, where it is negative and positive, respectively, as visible in figure 16-(a). Examination of simulation results at several Reynolds numbers, indicates that both the wavelength and the vertical

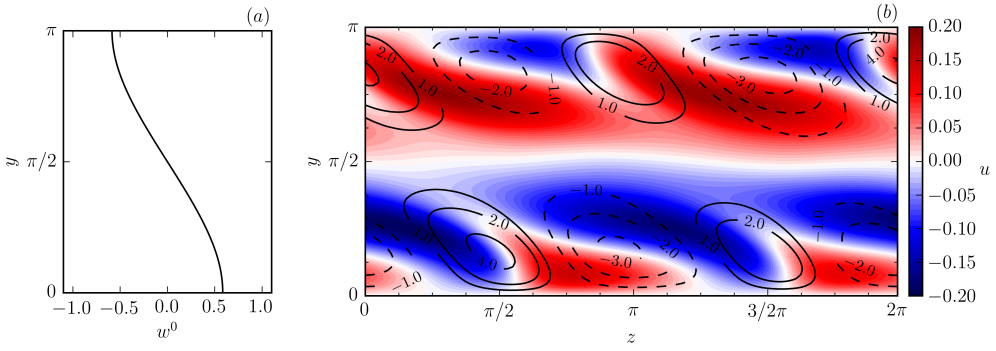

Figure 16: (a): mean axial velocity during the transient decay at $t = 260$. (b): spatial structure of the travelling wave pattern at $t = 260$. The colour map shows the azimuthal velocity component u, while contour lines indicate $100\psi'$, i.e. the local perturbation of the streamfunction with respect to the mean axial flow.

extension of such structures decrease as the Reynolds number increases. Interestingly, we have been have to track down this travelling wave solution at Reynolds number as low as 24, by slowly reducing with time the Reynolds number.

The spatial structure of ψ' suggests that the travelling wave pattern consists of packets of small scale azimuthal vortices with azimuthal vorticity of alternating sign, located close to the boundaries and moving along the axial direction. The weak rotation of the vortices generates an associated structure of high and low speed streaks of u. Considering the lower boundary, when the rotation of two adjacent vortices produces an upward motion, low speed fluid is ejected from the boundary, whereas in regions where the rotation of the vortices induces a motion towards the boundary and a high speed streak is observed.

The structure of the streak and of the vortices appears highly distorted, as a consequence of the inherent convective nature of these flow structures. Animated flow sequences reveal that the convective velocity as these structures has the same sign of the mean axial velocity, thus it is positive for $y < \pi/2$ and negative for $y > \pi/2$. Numerical values of the convective velocity across the entire height of the domain and during a large fraction of the transient decay were computed by a cross-correlation analysis. Briefly, for each y, short time series of $u(y, t)$ where taken at points $z = 0$ and $z = \pi/4$. The length of the time series was long enough to capture the signature of at least two repeated structures, i.e. twice the ratio wavelength to propagation velocity, and short enough with respect to the variations in time of the mean flow properties. Cross-correlation analysis

of the two signals provided the time lag of maximum correlation, which together with the spacing between the two measurement points provided an estimate of the propagation velocity. We observed that the convective velocity was essentially constant along the transient decay, as opposed to the decay of the mean flow value. In addition, it presented a step-like behaviour along y: it was positive and almost constant for $y < \pi/2$ and negative for $y > \pi/2$, but showed a sharp variation at $\pi/2$, in contrast to the smooth variation of the convective axial velocity. This feature suggests that the travelling wave pattern is not distorted by the mean shear but travels on top of it. The value of the convective velocity was significantly higher than the mean flow speed. At $t = 260$, to which the results of figure 16 refer, the convective velocity was about 3.5, so about five times larger then the mean component.

5. Conclusions

In this paper we have derived and characterised a simplified model of the well known Taylor-Couette flow. The dynamics are parametrized by two nondimensional numbers, the Reynolds number, determining the shear rate, and the rotation number, describing the effect of the system rotation and of the associated Coriolis force. The objective of the paper is to construct a model flow that can be used as flexible test bed for developing novel analysis methods for stability, transition and control. For instance, a novel method for proving global stability of a fluid flow, (Chernyshenko et al. (2014); Huang et al. (2015)), has been applied on this system. To facilitate such studies we have introduced a number of assumptions in the derivation of the model that make the system easily amenable to mathematical analysis, although the connection with the physics of the full three dimensional Taylor-Couette problem is, some times, partially loose. The important feature of the present model is that in contrast to other models of the Taylor-Couette flow based on ordinary differential equations, this model is still given by a set of partial differential equations. These describe the evolution of axisymmetric velocity perturbations in a thin region occupying the middle of the annulus between the two cylinders, in a narrow gap limit of the governing equations. In contrast to many previous works, periodic boundary conditions along the radial direction are applied to the problem. This seemingly unphysical choice is justified by the requirement to simplify the mathemati-

cal analysis of the problem. For instance, the linear and energy stability problems can be solved analytically in the present case, whereas they require a numerical solution in the more common case of no-slip boundary conditions. Different types of symmetry constraints, along the radial and axial direction, are also enforced on the flow variables.

We have presented numerical results to highlight the range of behaviour that this simple model flow displays. Without symmetry constraints along the radial direction, the system possesses a set of degenerate normal modes that can grow unbounded in nonlinear simulations of the flow. It can be argued that these modes describe physically the growth of large scale Taylor vortices in the full gap. When symmetry constraints are applied along both the radial and the axial directions, the flow shows a first bifurcation resulting in the well known Taylor vortex pattern. Linear stability analysis of this secondary flow shows that such flow structure is linearly stable at all Reynolds numbers, owing to the high symmetry of the problem and to the assumption of axisymmetric perturbations. This is in contrast with the occurrence of tertiary time-periodic states for the three dimensional flow such as the wavy vortex pattern, which arises as a Hopf-type bifurcation of the secondary state.

If symmetry constraints are applied along the radial direction only, the steady Taylor vortices show a sub-critical Hopf-type secondary bifurcation. In simulations of this sub-critical regime, the flow displays a chaotic motion, with a pattern that appears to repeat in time with a relatively long period. This pattern is characterised by the exponential decay of an intense axial motion over which wave-like disturbances travel along the axial direction. The spatial structure of these waves is a packet of weak and small scale azimuthal vortices travelling along the upper and lower boundaries of the domain in opposite directions. The rotation induced by the vortices, confined near the boundaries in regions which decrease in height with the Reynolds number, also generate an associated pattern of low and high azimuthal velocity streaks. This regime appears to be unstable as the exponential decay of the kinetic energy of this motion is erratically interrupted by an intense flow mixing and reorganisation of the structure.

Acknowledgments

Funding from EPSRC under the grants EP/J011126/1 and EP/J010073/1 and support from Airbus Operation Ltd., ETH Zurich (Automatic Control Laboratory), University of Michigan (Department of Mathematics), and University of California, Santa Barbara (Department of Mechanical Engineering) are gratefully acknowledged.

Ahmadi, M., Valmorbida, G., Papachristodouidou, A., 2015. A convex approach to hydrodynamic analysis. In: Decision and Control (CDC), 2015 IEEE 54th Annual Conference on.

Andereck, C. D., Dickman, R., Swinney, H. L., 1983. New flows in a circular Couette system with co-rotating cylinders. Phys. Fluids 26 (6), 1395–1401.

Andereck, C. D., Liu, S. S., Swinney, H. L., 1986. Flow regimes in a circular Couette system with independently rotating cylinders. J. Fluid Mech. 164, 155–183.

Barenghi, C., Jones, C., 1989. Modulated Taylor–Couette flow. J. Fluid Mech. 208, 127–160.

Bech, K. H., Andersson, H. I., 1996. Secondary flow in weakly rotating turbulent plane Couette flow. J. Fluid Mech. 317, 195–214.

Bech, K. H., Andersson, H. I., 1997. Turbulent plane Couette flow subject to strong system rotation. J. Fluid Mech. 347, 289–314.

Boyd, J. P., 2001. Chebyshev and Fourier spectral methods. Courier Corporation.

Brauckmann, H. J., Eckhardt, B., 2013. Direct numerical simulations of local and global torque in Taylor–Couette flow up to Re=30000. J. Fluid Mech. 718, 398–427.

Brauckmann, H. J., Salewski, M., Eckhardt, B., 2015. Momentum transport in Taylor-Couette flow with vanishing curvature.

Busse, F. H., 2012. Viewpoint: The twins of turbulence research. Physics 5.

Canuto, C., Hussaini, M. Y., Quarteroni, A., Zang, T. A., 2007. Spectral methods: evolution to complex geometries and applications to fluid dynamics. Springer.

Chernyshenko, S. I., Goulart, P., Huang, D., Papachristodouidou, A., 2014. Polynomial sum of squares in fluid dynamics: a review with a look ahead. Philos. Trans. R. Soc. Lond., A 372.

Chossat, P., Iooss, G., 1985. Primary and secondary bifurcations in the Couette-Taylor problem. Jpn. J. Ind. Appl. Math. 2 (1), 37–68.

Coles, D., 1965. Transition in circular Couette flow. J. Fluid Mech. 21, 385–425.

Daviaud, F., Hegseth, J., Bergé, P., 1992. Subcritical transition to turbulence in plane Couette flow. Phys. Rev. Lett. 69 (17), 2511–2514.

Doering, C. R., Gibbon, J. D., 1995. Applied analysis of the Navier-Stokes equations. Vol. 12. Cambridge Univ. Press.

Dong, S., 2008. Turbulent flow between counter-rotating concentric cylinders: a direct numerical simulation study. J. Fluid Mech. 615, 371–399.

Donnelly, R., Simon, N., 1960. An empirical torque relation for supercritical flow between rotating cylinders. J. Fluid Mech. 7 (03), 401–418.

Drazin, P. G., Reid, W. H., 2004. Hydrodynamic stability. Cambridge Univ. Press.

Eckhardt, B., Grossmann, S., Lohse, D., 2007. Torque scaling in turbulent Taylor–Couette flow between independently rotating cylinders. J. Fluid Mech. 581, 221–250.

Faisst, H., Eckhardt, B., 2000. Transition from the Couette-Taylor system to the plane Couette system. Physical Review E 61 (6), 7227–7230.

Fasel, H., Booz, O., 1984. Numerical investigation of supercritical Taylor-vortex flow for a wide gap. J. Fluid Mech. 138, 21–52.

Goulart, P. J., Chernyshenko, S., 2012. Global stability analysis of fluid flows using sum-of-squares. Phys. D 241 (6), 692–704.

Grossmann, S., Lohse, D., 2011. Multiple scaling in the ultimate regime of thermal convection. Phys. Fluids 23 (4), 045108.

Huang, D., Chernyshenko, S., Goulart, P., Lasagna, D., Tutty, O., Fuentes, F., 2015. Sum-of-squares of polynomials approach to nonlinear stability of fluid flows: an example of application. Accepted on Philos. Trans. R. Soc. Lond., A.

Huisman, S. G., van der Veen, R. C. A., Sun, C., Lohse, D., 2014. Multiple states in highly turbulent Taylor–Couette flow. Nat. Commun. 5.

Huisman, S. G., van Gils, D. P. M., Grossmann, S., Sun, C., Lohse, D., 2012. Ultimate turbulent Taylor-Couette flow. Phys. Rev. Lett. 108 (2), 024501.

Jones, C., 1982. On flow between counter-rotating cylinders. J. Fluid Mech. 120, 433–450.

Joseph, D. D., Hung, W., 1971. Contributions to the nonlinear theory of stability of viscous flow in pipes and between rotating cylinders. Arch. Ration. Mech. Anal. 44 (1), 1–22.

King, G. P., Li, Y., Lee, W., Swinney, H. L., Marcus, P. S., 1984. Wave speeds in wavy Taylor-vortex flow. J. Fluid Mech. 141, 365–390.

Kuhlmann, H., 1985. Model for Taylor-Couette flow. Phys. Rev. A 32 (3), 1703.

Lezius, D. K., Johnston, J. P., 1976. Roll-cell instabilities in rotating laminar and trubulent channel flows. J. Fluid Mech. 77 (01), 153–174.

Marcus, P. S., 1984. Simulation of Taylor-Couette flow. Part 2. Numerical results for wavy-vortex flow with one travelling wave. J. Fluid Mech. 146, 65–113.

Martínez-Arias, B., Peixinho, J., Crumeyrolle, O., Mutabazi, I., 2014. Effect of the number of vortices on the torque scaling in Taylor–Couette flow. J. Fluid Mech. 748, 756–767.

Nagata, M., 1986. Bifurcations in Couette flow between almost corotating cylinders. J. Fluid Mech. 169, 229–250.

Nagata, M., 1988. On wavy instabilities of the Taylor-vortex flow between corotating cylinders. J. Fluid Mech. 188.

Nagata, M., 1990. Three-dimensional finite-amplitude solutions in plane Couette flow: bifurcation from infinity. J. Fluid Mech. 217, 519–527.

Nagata, M., 1998. Tertiary solutions and their stability in rotating plane Couette flow. J. Fluid Mech. 358, 357–378.

Ostilla-Mónico, R., Stevens, R. J., Grossmann, S., Verzicco, R., Lohse, D., 2013. Optimal Taylor–Couette flow: direct numerical simulations. J. Fluid Mech. 719, 14–46.

Ostilla-Mónico, R., van der Poel, E. P., Verzicco, R., Grossmann, S., Lohse, D., 2014. Exploring the phase diagram of fully turbulent Taylor–Couette flow. J. Fluid Mech. 761, 1–26.

Ostilla-Mónico, R., Verzicco, R., Grossmann, S., Lohse, D., 2015. The effect of Taylor rolls on highly turbulent Taylor–Couette flow. arXiv preprint arXiv:1501. 03012.

Paoletti, M. S., Lathrop, D. P., 2011. Angular momentum transport in turbulent flow between independently rotating cylinders. Phys. Rev. Lett. 106 (2), 024501.

Prigent, A., Grégoire, G., Chaté, H., Dauchot, O., van Saarloos, W., 2002. Large-scale finite-wavelength modulation within turbulent shear flows. Phys. Rev. Lett. 89 (1), 014501.

Salewski, M., Eckhardt, B., 2015. Turbulent states in plane Couette flow with rotation. Phys. Fluids 27 (4), 045109.

Schmid, P. J., 2010. Dynamic mode decomposition of numerical and experimental data. J. Fluid Mech. 656, 5–28.

Smith, G. D., 1985. Numerical solution of partial differential equations: finite difference methods. Oxford University Press.

Speziale, C., Wilson, M., 1989. Numerical study of plane Couette flow in a rotating framework. Acta Mech. 77 (3-4), 261–280.

Taylor, G. I., 1923. Stability of a viscous liquid contained between two rotating cylinders. Philos. Trans. R. Soc. Lond., A. 223 (605-615), 289–343.

Tillmark, N., Alfredsson, P. H., 1991. An experimental study of transition in plane Couette flow. In: Advances in Turbulence 3. Springer Berlin Heidelberg, pp. 235–242.

Tillmark, N., Alfredsson, P. H., 1992. Experiments on transition in plane Couette flow. J. Fluid Mech. 235, 89–102.

Tsukahara, T., Tillmark, N., Alfredsson, P. H., 2010. Flow regimes in a plane Couette flow with system rotation. J. Fluid Mech. 648, 5–33.